Economic and Risk Assessment - Techno-economic Risk Assessment (Part II)

Donald and Tarnagulla Microgrid Feasibility Study

Prepared for: Centre for New Energy Technologies (C4NET), Powercor

Acknowledgment: Powercor provided a network map and data and continuous feedback

from the University of Melbourne

Submitted by: Tossaporn Surinkaew, Dr Rakibuzzaman Shah, and Professor Syed Islam

Research Team: Carmen Bas Domenech, Antonella maria De Corato, Prof Pierluigi Mancarella, Dr Maria Vrakopoulou, Tossaporn Surinkaaew, Dr Rakibuzzaman Shah, Professor Syed Islam

Organisation: Federation University Australia

Partner: The University of Melbourne

This project was supported by the Department of Industry, Science, Energy and Resources and C4NET.

Executive Summary

The Donald and Tarnagulla Microgrid Feasibility Study has been launched under a Grant Agreement between the Centre for New Energy Technologies Limited (C4NET) and the Commonwealth of Australia, represented by the Department of Industry, Science, Energy and Resources (DISER).

The study includes 12 interdisciplinary projects where Project 8, “Economic and Risk Assessment”, aims to develop microgrid investment and operational models to analyse the impacts the investment in distributed energy resources comprising the microgrid will have on the different stakeholders. This includes economic impact, value and opportunities created, and risks for all grid users, distribution network service providers, aggregators, and retailers during the lifetime of the microgrid.

Project 8 was performed by a collaboration between the University of Melbourne and Federation University. This report (“Project 8: Economic and Risk Assessment – Part II”) presents the work performed by the Federation University Australia focused on network reliability and the impact of bushfires in each town. This report covers Task 3 and Task 5 (part of) of Project 8: Economic and Risk Assessment.

This work presents a risk assessment model based on distribution network reliability assessment techniques to value the techno-economic risk associated with microgrid users for different planning alternatives and types of events (e.g., bushfires). The detailed modeling of bushfires has been considered in this work. Moreover, this work presents an artificial intelligent-based techno-economic risk-based assessment of a microgrid considering the effects of firestorm dynamics. Here, a developed firestorm model is constructed from bushfire and wind models. An artificial intelligent-based method, namely, the physics-informed deep-learning neural network, is applied to predict *D*-day-ahead firestorm-inducted factors, i.e., forest fire danger index and wind speed vectors.

The economic risk valuation for specific microgrids has been fed back to the investment model for comparison. The detailed assessment results can be found in (“Project 8: Economic and Risk Assessment – Part I”).

Contents

List of Figures

List of Tables

Glossary

Abbreviation	Definition
AER	Australian Energy Regulator
BAU	Business as usual
DNN	Deep-learning neural network
EENS	Expect energy not supplied
FFDI	Forest fire danger index
HILP	High-impact low-probability
MV	Medium voltage
VCR	Value of customer reliability

1. Project Background and Objectives

C4NET, in collaboration with Powercor and Central Victorian Greenhouse Alliance, have been engaged in the study to improve the electricity access and supply in two regional Victorian towns of Donald and Tarnagulla. Through a series of projects, the consortium aims to understand and analyse the possibilities of improving electricity generation and supply in the region by determining and implementing innovative technical and economic solutions.

This project is part of a larger study to assess partial or full microgrid feasibility in two regional Victorian towns with supply vulnerabilities. The network operators and the community groups in these two towns have been interested in improving the reliability of their power supply by enabling cost-effective fully or partially self-sustaining microgrids through alternative energy resources such as solar and battery storage(s). Federation University Australia in collaboration with C4NET and Powercor have conducted the risk analysis of microgrid facilities at “Donald” and “Tarnagulla”.

Low-probability high-impact (HILP) events such as bushfire and wildfire in Australia, are inevitable and unpredictable. Besides, uncertainties from distributed renewable energy resources may prevent conventional techniques to improve reliability of power grids. This project aims at modeling a new dynamic bushfire model for reliability assessment. In this project, the Donald and Tarnagulla microgrids are created in DIgSILENT PowerFactory. Different from previous study, the new dynamic bushfire is mathematically modelled in MATLAB, the Monte Carlo Simulation is applied to generate the outage contingency (i.e., *N*-1 contingency, *N*-2 contingency, or *N-K* contingency). After that the obtained outage scenarios are used as inputs to DIgSILENT PowerFactory to evaluate the expected energy not supplied (EENS). Next, the EENSs obtained from the previous stage are used to find the values of customer reliability. Simulation results are analysed and conducted in several dynamic bushfire conditions and operating points to demonstrate their effects on the reliability of the Donald and Tarnagulla microgrids.

2. Task Descriptions

The aim of this project is to assess the reliability with specific techno-economic risk indices (e.g., expected-energy-not-supplied, value-of-customer-reliability) under extreme conditions.

The timeline of the project is provided below:

3. System Modeling and Methodology

3.1. Donald and Tarnagulla Networks

A single line diagram of Donald town connected to the electricity grid is given in Figure 1. It can be observed that the Donald is connected to the main grid through the Charlton zonal substation by the medium voltage (MV) line (denoted as Donald line for this study). There are a number of load points along the Donald line. There are several loads connected in those areas. Therefore, the actual system model development for those areas is also vital to study the reliability and quality of supply. Using lumped loads for these areas might not give accurate results. Detailed models of the Donald line, Donald town, Litchfield area, and Donald South area are developed in DIgSILENT Power Factory software. *This model has been considered as the base case for the Donald network* (*i.e., business as usual (BAU) case*). For the Tarnagulla network, it is located at the end of the incoming feeder (single line diagram of Tarnagulla is given in Figure 2). There are no other areas that are being fed via Tarnagulla. Therefore, only Tarnagulla town is modelled for the reliability study. This model has been considered as the base case for the Tarnagulla network (i.e., BAU case). In this project, the Donald and Tarnagulla networks are used as the study systems to investigate the effects of dynamic bushfire on value of customer reliability (VCR).

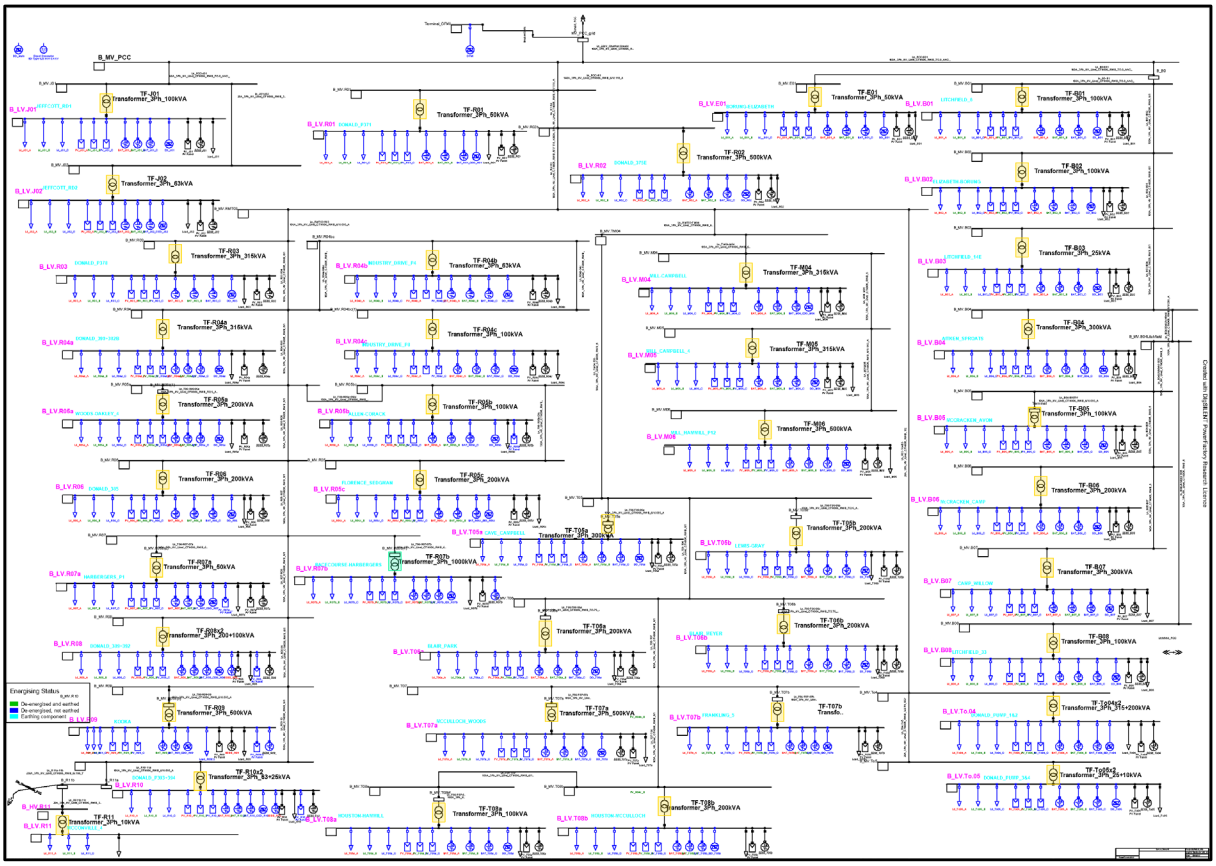

Figure 1: Single line diagram of Donald distribution network

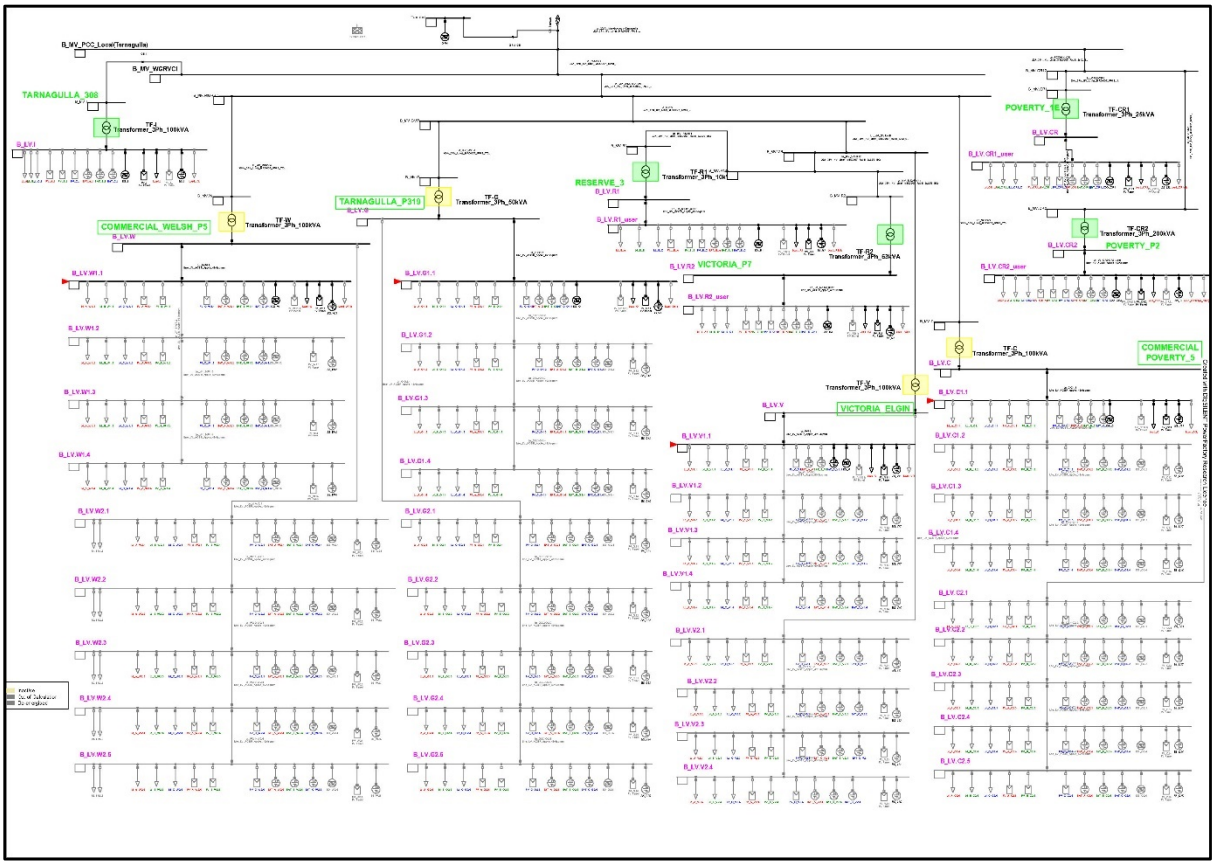

Figure 2: Single line diagram of Tarnagulla distribution network.

3.2. Formulation of $FFDI$ in Time-Series Data

The forest fire danger index ($FFDI$) in time-domain is adopted from [1],

$$FFDI(t) = 1.2753e^{(0.987\log DF(t)+0.0338T(t)+0.0234v_w(t)-0.0345RH(t))} \quad (1)$$

where t is the time, DF is the drought factors, T is the air temperature, v_w is the wind speed, and RH is the relative humidity in percent.

It should be noted that the Griffiths formulation [2] is used to estimate the DF, while the soil moisture deficit is calculated by the Keetch-Byram index [3]. The levels of bushfire weather risk defined based on the value range of FFDI that are currently used in Victoria is shown in Figure 3.

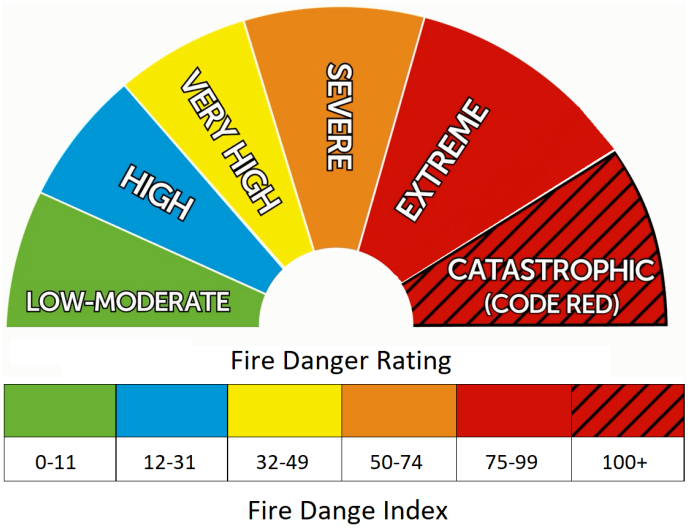

Figure 3: Fire danger rating.

Table II shows the monthly climate statistics used for calculating and estimating the $FFDI$ in which the real-time data can be downloaded from http://www.bom.gov.au/climate. Here, red, green, and yellow highlights are the data used to calculate the $FFDI$. Figures 4, 5, 6, and 7 illustrate the minimum and maximum temperatures, relative humidity, and wind speed, respectively. By considering (1), the probability of high $FFDI$ will occur, when the DF, T, and v_w increase while the RH decreases. Alternatively, one can consider $FFDI \propto \left(DF, T, v_w, \frac{1}{RH}\right)$. For this reason, the maximum temperature T, drought factor DF, and wind speed v_w, and minimum relative humidity RH are used to evaluate the $FFDI$. By using (1), Figure 6 demonstrates the maximum $FFDI$ at 9 am and 3 pm. As mentioned by [4], the probability of line failure is constant when $FFDI < 11$ while the probability of line failure is variable when $FFDI \geq 11$. As can be observed in Figure 6, the line failure rate is constant at $FFDI$ at 9 am in all months. For the $FFDI$ at 3 pm, the $FFDI$ is constant around mid of March to mid of October, while the $FFDI$ is constant is variable in other periods. Moreover, the increment of length of feeders/transmission lines leads to higher probability of failure. This factor will be considered in the construction of the fragility curve in the next section.

Table 1 Monthly climate statistics at Essen Don Airport collected from 1939 to July 2022, created on 13 July 2022.

Monthly Climate Statistics for 'ESSENDON AIRPORT' [086038]																
Created on [13 Jul 2022 14:29:41 GMT+00:00]																
086038 ESSENDON AIRPORT																
Commenced: 1929																
Last Record: 2022																
Latitude: 37.73 Degrees South																
Longitude: 144.91 Degrees East																
Elevation: 78 m																
State: VIC																
Statistic Element	January	February	March	April	May	June	July	August	Septembe	October	Novembe	Decembe	Annual	Number o	Start Year	End Year
Mean maximum temperature (Degrees C) for years 1939 to 2	26.6	25.9	24.1	20.2	16.4	13.8	13.2	14.4	16.9	19.5	22	24.6	19.8	53	1939	2022
Highest temperature (Degrees C) for years 1939 to 2022	45.8	47.3	40.7	35.2	26.7	22.6	21.9	24.4	30.3	36.4	41.5	44.4	47.3	53	1939	2022
Date of Highest temperature for years 1939 to 2022	31-Jan-68	7-Feb-09	4-Mar-42	########	4-May-67	8-Jun-05	18-Jul-13	########	########	12-Oct-06	########	########	7-Feb-09	N/A		1939	2022
Lowest maximum temperature (Degrees C) for years 1939 to	14.7	13.9	13.6	10.6	8.4	6.7	6.1	6.8	8.3	10	11.3	12.5	6.1	53	1939	2022
Date of Lowest maximum temperature for years 1939 to 202	2-Jan-41	########	########	########	########	22-Jun-50	2-Jul-68	9-Aug-51	########	1-Oct-57	########	########	2-Jul-68	N/A		1939	2022
Decile 1 maximum temperature (Degrees C) for years 1939 t	19.6	19.3	18.2	15.2	12.9	11.2	10.6	11.4	12.8	14.3	15.9	17.8		53	1939	2022
Decile 9 maximum temperature (Degrees C) for years 1939 t	36.1	34.1	31.5	26.4	20.3	16.6	15.7	17.8	21.6	26	30	34		53	1939	2022
Mean number of days >= 30 Degrees C for years 1939 to 2022	8.9	7	4.9	0.5	0	0	0	0	0	0.8	3.1	6.2	31.4	53	1939	2022
Mean number of days >= 35 Degrees C for years 1939 to 2022	4	2.3	1	0	0	0	0	0	0	0.1	0.5	2.3	10.2	53	1939	2022
Mean number of days >= 40 Degrees C for years 1939 to 2022	0.9	0.2	0.1	0	0	0	0	0	0	0	0	0.4	1.6	53	1939	2022
Mean minimum temperature (Degrees C) for years 1939 to 2	13.8	14.1	12.7	10.1	7.9	6.1	5.5	5.7	6.9	8.4	10.2	12	9.5	53	1939	2022
Lowest temperature (Degrees C) for years 1939 to 2022	5.7	5.3	3.7	0.6	0.1	-3.3	-2.6	-2.4	-1.6	-0.3	2.2	4	-3.3	53	1939	2022
Date of Lowest temperature for years 1939 to 2022	22-Jan-40	########	########	########	########	17-Jun-69	4-Jul-63	########	########	9-Oct-39	4-Nov-70	3-Dec-55	17-Jun-69	N/A		1939	2022
Highest minimum temperature (Degrees C) for years 1939 to	28.8	26.2	25.3	22.5	17.1	13.1	13.2	14.7	18.6	21.3	22.7	26.2	28.8	53	1939	2022
Date of Highest minimum temperature for years 1939 to 202	15-Jan-14	########	########	2-Apr-14	3-May-42	1-Jun-13	19-Jul-13	4-Aug-11	3-Sep-21	28-Oct-07	########	########	15-Jan-14	N/A		1939	2022
Decile 1 minimum temperature (Degrees C) for years 1939 t	9.8	10	8.4	6	3.8	2.1	1.7	2.3	2.9	4.4	6.1	8.1		53	1939	2022
Decile 9 minimum temperature (Degrees C) for years 1939 t	18.2	18	17	14.1	11.9	9.6	8.8	9.1	10.8	12.8	14.8	16.2		53	1939	2022
Mean number of days <= 2 Degrees C for years 1939 to 2022	0	0	0	0	0.7	2.8	3.6	2.6	1.4	0.3	0	0	11.4	53	1939	2022
Mean number of days <= 0 Degrees C for years 1939 to 2022	0	0	0	0	0	0.6	1	0.6	0.2	0	0	0	2.4	53	1939	2022
Mean daily ground minimum temperature Degrees C for yea																
Lowest ground temperature Degrees C for years null to null																
Date of Lowest ground temperature for years null to null														N/A		
Mean number of days ground min. temp. <= -1 Degrees C for																
Mean rainfall (mm) for years 1929 to 2022	43.7	43.9	39.5	54.6	48.7	40.4	42.8	48.1	50.8	59.3	58.5	51.4	585.7	73	1929	2022
Highest rainfall (mm) for years 1929 to 2022	224.1	195.5	154.1	162.7	140.1	115	101.9	99	113	153.6	183.6	152.7	817.9	76	1929	2022
Date of Highest rainfall for years 1929 to 2022	1963	1973	1970	1935	1974	2013	1936	1975	1960	1934	1954	1933	1974	N/A	1929	2022
Lowest rainfall (mm) for years 1929 to 2022	0.4	0.5	1.9	6.6	3.3	8	12.8	14.8	11	6.8	7	1.3	350.4	76	1929	2022
Date of Lowest rainfall for years 1929 to 2022	2009	1965	1948	2019	1934	1974	1979	2011	2008	2006	1937	1972	1938	N/A	1929	2022
Decile 1 monthly rainfall (mm) for years 1929 to 2022	9.4	3.7	9.2	15.4	16.7	17.7	19.6	24.1	18.3	18.5	25	15.6	423.4	76	1929	2022
Decile 5 (median) monthly rainfall (mm) for years 1929 to 20	32.5	33	32.9	45.2	47.4	35.1	40.4	45.4	48.4	56.3	48	44.8	604	76	1929	2022
Decile 9 monthly rainfall (mm) for years 1929 to 2022	79.4	102.6	78.7	116.6	83	65.5	67.3	72.7	86.2	113.9	110.3	94.7	757.5	76	1929	2022
Highest daily rainfall (mm) for years 1929 to 2022	112.8	118	67.6	100	58.4	68.6	42.7	34.4	54	89.4	89.4	52.6	118	68	1929	2022
Date of Highest daily rainfall for years 1929 to 2022	29-Jan-63	3-Feb-05	########	8-Apr-77	########	1-Jun-13	11-Jul-33	########	########	16-Oct-83	########	########	3-Feb-05	N/A		1929	2022
Mean number of days of rain for years 1929 to 2022	7.4	7.3	8.8	11	13.3	13.6	15.2	15.7	14.3	13.1	11.7	10.1	141.5	76	1929	2022
Mean number of days of rain >= 1 mm for years 1929 to 2022	4.4	4.2	5.2	6.8	7.4	7.2	7.7	8.8	8	7.7	7	6.1	80.5	68	1929	2022
Mean number of days of rain >= 10 mm for years 1929 to 202	1.2	1.1	0.9	1.5	1.2	0.8	0.6	0.8	1.1	1.5	1.5	1.4	13.6	68	1929	2022
Mean number of days of rain >= 25 mm for years 1929 to 202	0.3	0.3	0.2	0.4	0.1	0	0.1	0.1	0.1	0.2	0.3	0.3	2.4	68	1929	2022
Mean daily wind run (km) for years 2003 to 2022	404	380	366	323	344	334	390	410	414	393	394	401	379	18	2003	2022
Maximum wind gust speed (km/h) for years 1939 to 2022	117	117	115	108	100	106	124	130	147	121	115	122	147	52	1939	2022
Date of Maximum wind gust speed for years 1939 to 2022	4-Jan-46	########	########	8-Apr-66	########	10-Jun-47	1-Jul-42	4-Aug-47	6-Sep-48	21-Oct-48	########	########	6-Sep-48	N/A		1939	2022
Mean daily sunshine (hours) for years null to null																
Mean daily solar exposure (MJ/(m*m)) for years 1990 to 202	24.1	20.9	16.3	11.2	7.7	6.3	7.1	9.9	13.4	17.8	21.2	23.9	15	33	1990	2022
Mean number of clear days for years 1939 to 2010	6.6	5.7	6.4	4.1	3.2	3.1	2.8	3.2	4	3.6	3.1	4.7	50.5	34	1939	2010
Mean number of cloudy days for years 1939 to 2010	11	10.7	12.3	14.8	18	17.1	17	15.3	14.4	17	16.9	14.3	178.8	34	1939	2010
Mean daily evaporation (mm) for years null to null																
Mean 9am temperature (Degrees C) for years 1939 to 2010	19.1	18.7	17.1	14.1	10.8	8.5	7.8	8.9	11.4	13.8	15.7	17.8	13.6	41	1939	2010
Mean 9am wet bulb temperature (Degrees C) for years 1939	14.5	14.8	13.6	11.5	9.2	7.3	6.5	7.3	8.9	10.5	12	13.3	10.8	37	1939	2010
Mean 9am dew point temperature (Degrees C) for years 194	10.6	11.9	10.7	9.1	7.6	6	5.1	5.5	6.3	7.3	8.3	9.5	8.2	29	1941	2010
Mean 9am relative humidity (%) for years 1941 to 2010	60	66	68	72	81	84	83	79	72	66	63	61	71	29	1941	2010
Mean 9am cloud cover (okas) for years 1939 to 2010	5	5.1	5	5.4	5.5	5.6	5.4	5.2	5.1	5.6	5.9	5.4	5.4	35	1939	2010
Mean 9am wind speed (km/h) for years 1939 to 2010	17.9	16.6	15.8	15	15	15.6	17.5	18.5	20.9	20.9	20	18.5	17.7	40	1939	2010
Mean 3pm temperature (Degrees C) for years 1939 to 2010	24.2	23.8	22.4	18.7	15.1	12.7	11.9	13.1	15.3	17.5	19.9	22.3	18.1	40	1939	2010
Mean 3pm wet bulb temperature (Degrees C) for years 1939	16.5	16.7	15.8	13.5	11.4	9.8	9	9.5	10.9	12.3	13.9	15.2	12.9	37	1939	2010
Mean 3pm dew point temperature (Degrees C) for years 194	10.3	11.4	10.1	8.6	7.6	6.6	5.6	5.6	6.2	7.3	8.2	9	8	28	1941	2010
Mean 3pm relative humidity (%) for years 1941 to 2010	46	49	48	53	62	67	66	62	57	54	50	47	55	28	1941	2010
Mean 3pm cloud cover (oktas) for years 1939 to 2010	4.1	4.4	4.6	5.4	5.8	5.8	5.8	5.5	5.4	5.5	5.5	4.9	5.2	34	1939	2010
Mean 3pm wind speed (km/h) for years 1939 to 2010	23.6	21.6	20.4	20.1	19.8	19.9	22	23.1	23.8	23.3	23.1	23.5	22	39	1939	2010
Averaged drought factor	10	9	9	8	7	7	7	7	8	8	9	10				

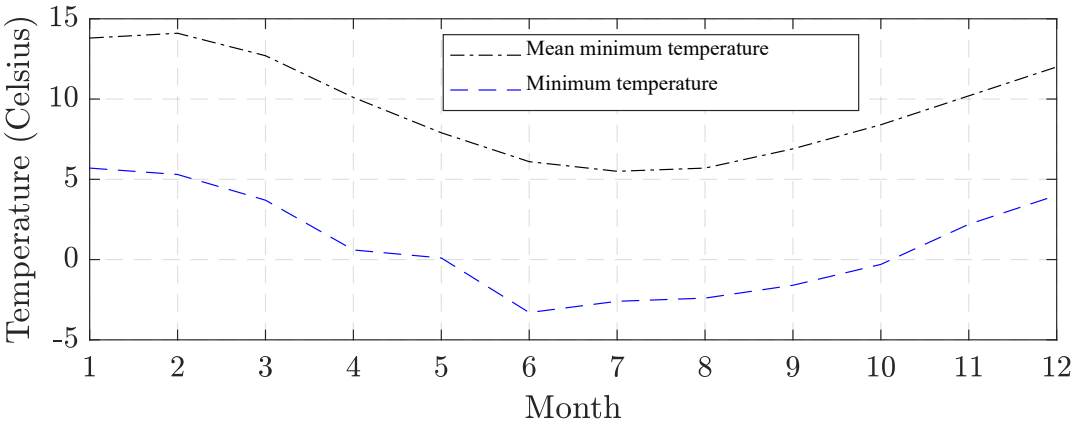

Figure 4: Time-series data of minimum temperature.

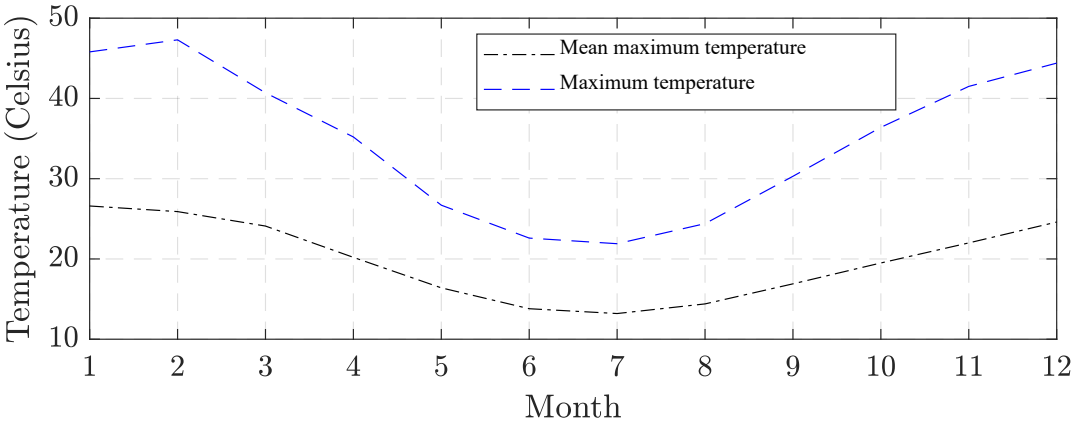

Figure 5: Time-series data of maximum temperature.

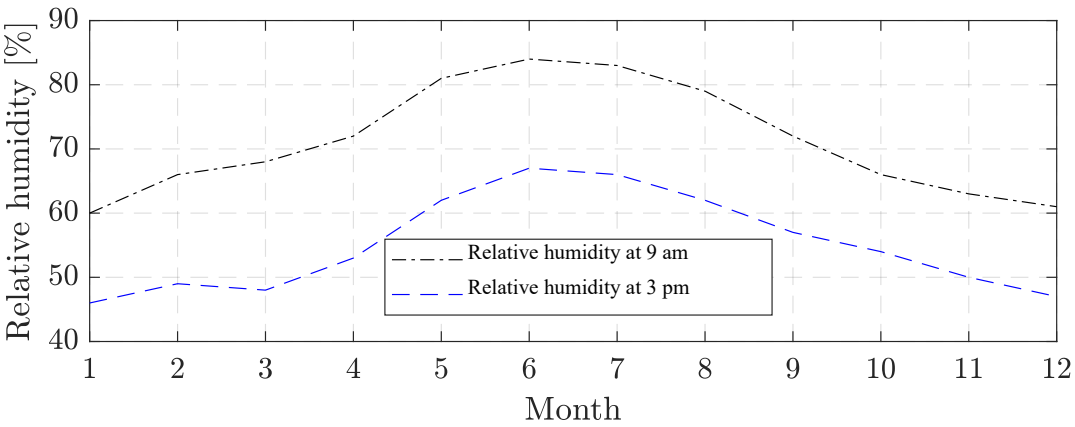

Figure 6: Time-series data of relative humidity.

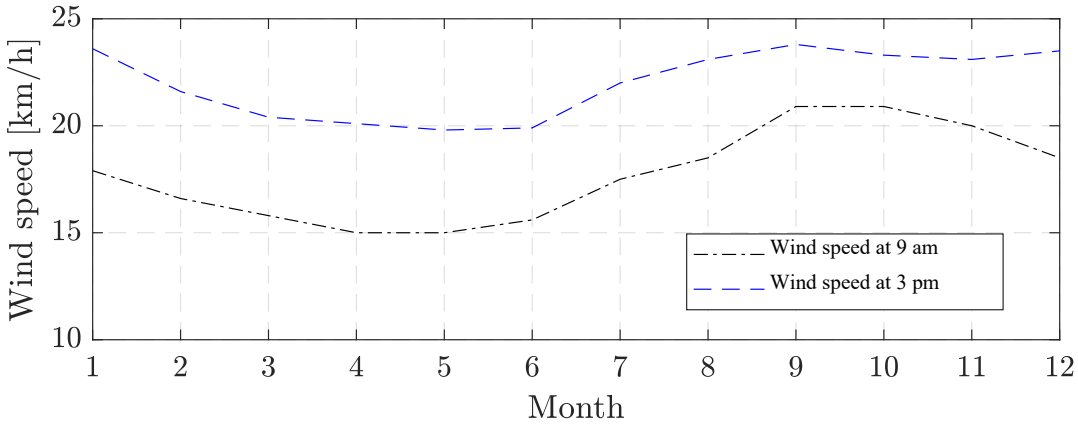

Figure 7: Time-series data of wind speed.

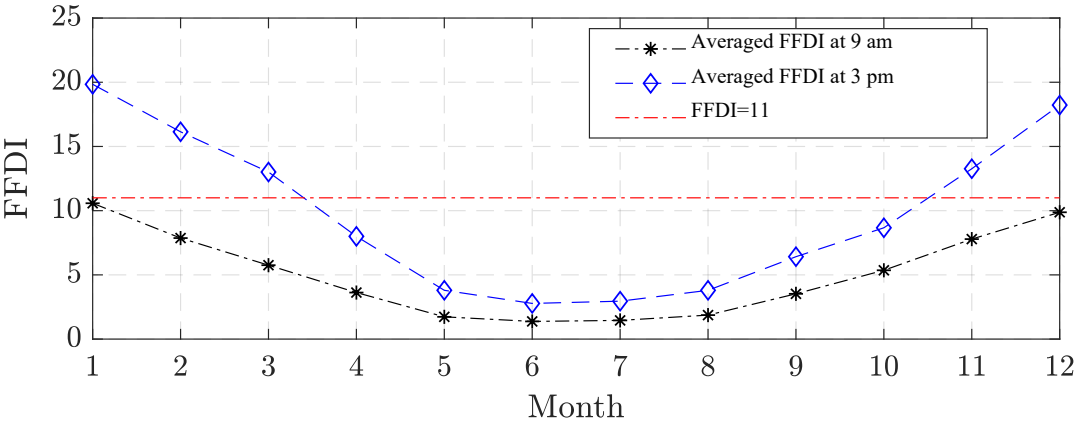

Figure 8: Time-series data of $FFDI$.

3.3. Construction and Analysis of Fragility Curve

The fragility curve is used to map the $FFDI$ with percentage of line failure (or line failure rate). As reported in **Project 7**, the line failure rate will keep constant when the $FFDI$ value is lower than 11. The initial failure rates and repair duration of different network, generation, and storage facilities are adopted from Table 38 in **Project 5**. As a result, the initial feeders/transmission lines failure rate (P_0) is equal to 0.0285/km, i.e., $P_0 = 0.0285/\text{km}$. For different feeder lengths, the vector of feeder lengths in km $(\mathbf{L}_{line})$ are obtained by,

$$\mathbf{L}_{line} = [L_1, L_2, \dots, L_{n_L}] \tag{2}$$

where subscripts $1, \dots, n_L$ are the line index.

Accordingly, the vector of initial feeder/transmission line failure rate considering $\mathbf{L}_{line}$ $(\mathbf{P}_{line,0})$ is formulated by,

$$\mathbf{P}_{line,0} = 0.0285 \times [L_1, L_2, \dots, L_{n_L}] \tag{3}$$

Let $st = 1, \dots, n_L$ be the st^{th} line index, the probability vector of failure based on the value of $FFDI$ for each feeder/transmission line $(\mathbf{P}_{FFDI}^{st})$ can be therefore obtained by,

$$\mathbf{P}_{FFDI}^{st} = \begin{cases} \mathbf{P}_{line,0}, & \text{if } FFDI < 11 \\ \mathbf{P}_{line,0} + \boldsymbol{m}\mathbf{P}_{line,0}(FFDI - 11), & \text{if } FFDI \geq 11 \end{cases} \tag{4}$$

where $\boldsymbol{m} = [m_1, m_2, \dots]$ is the sensitivity matrix in percent.

By using (11), Figures 9, 10, 11, 12, and 13 demonstrate the examples of different line failure probability considering the length of feeders/transmission lines, when $\boldsymbol{m} = [0.01, 0.02, \ldots, 0.05]$. Between $FFDI = 1$ and $FFDI = 11$, the failure probability is varied according to the length of line $\mathbf{L}_{line}$. On the other hand, when $FFDI > 11$, the failure probability directly increases depending on $\mathbf{L}_{line}$ and the sensitivity $\boldsymbol{m}$.

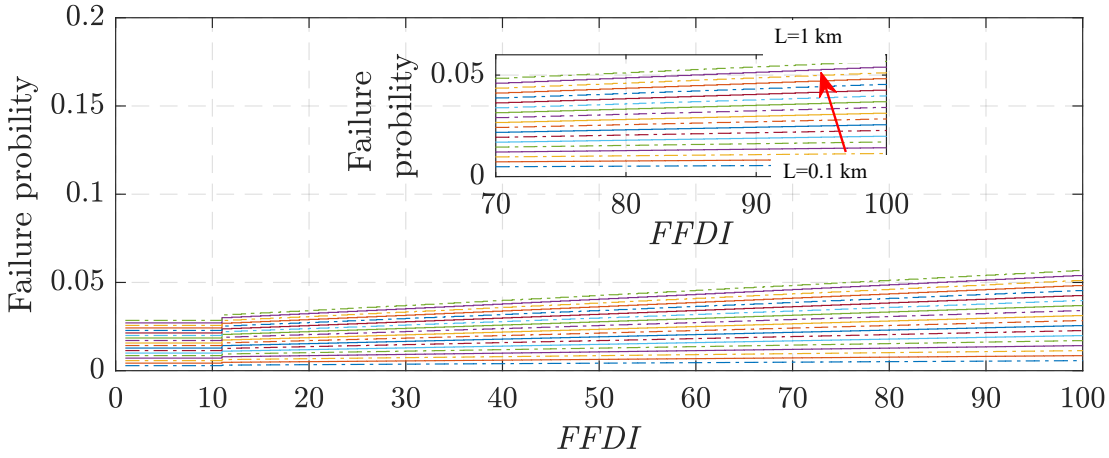

Figure 9: Fragility curve when $m_1 = 1\%$ (0.01).

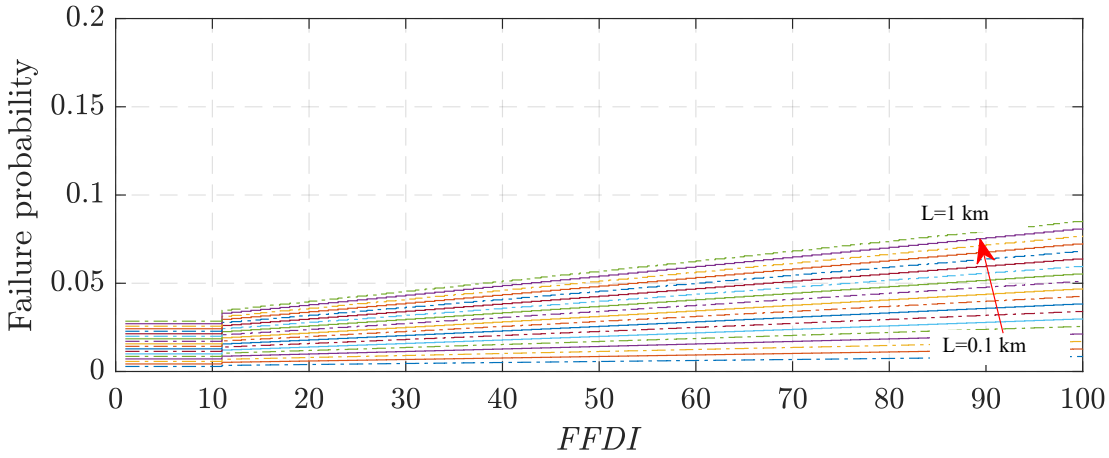

Figure 10: Fragility curve when $m_2 = 2\%$ (0.02).

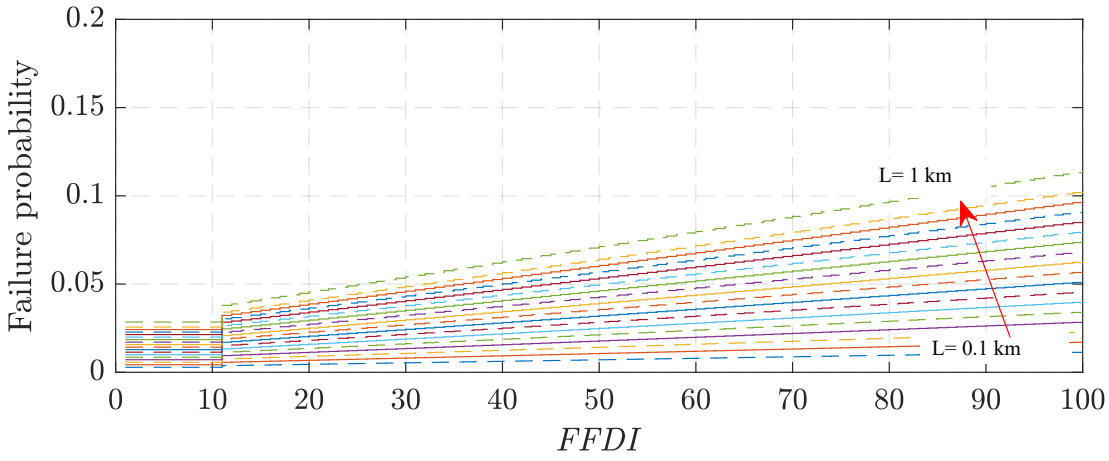

Figure 11: Fragility curve when $m_2 = 3\%$ (0.03).

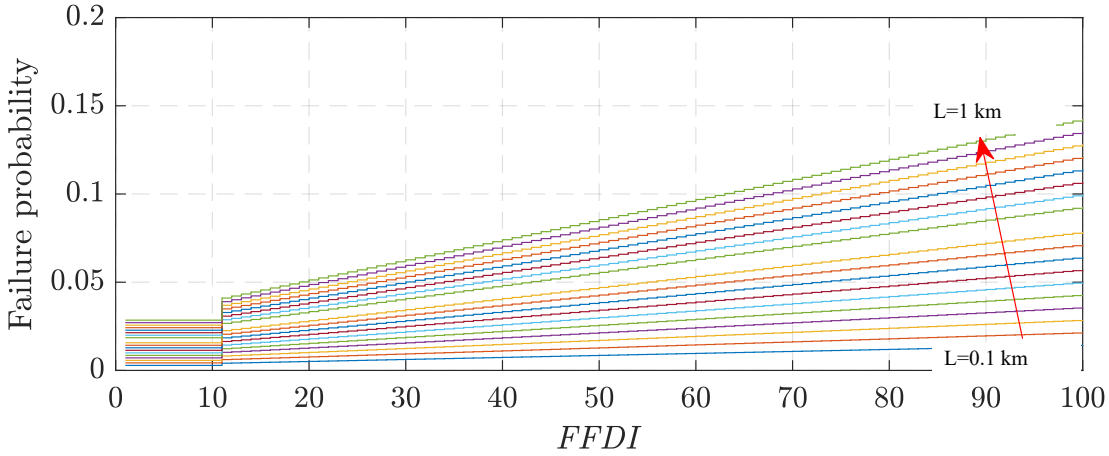

Figure 12: Fragility curve when $m_2 = 4\%$ (0.04).

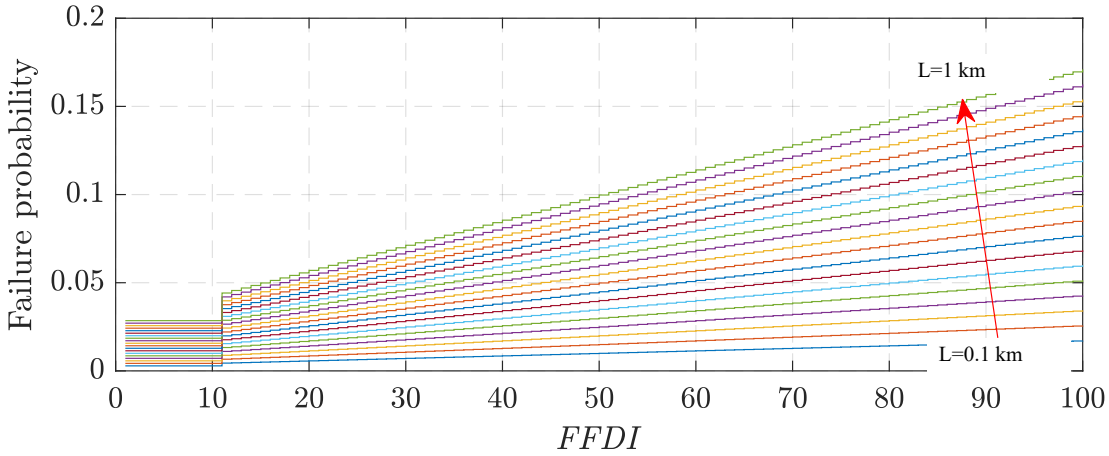

Figure 13: Fragility curve when $m_2 = 5\%$ (0.05).

Next, the time-series data of $FFDI$ in Figure 8 is used to construct the fragility curve. Accordingly, Figure 14 shows the fragility curve of $FFDI$ at 9 am. As can be seen, since the $FFDI$ is less than 11, the failure probability related to $FFDI$ is constant at each length of line (variable $\boldsymbol{m}$ is not matter). When the length of line increases, the failure probability increases. Figures 15, 16, 17, 18, and 19 depict the fragility curve of $FFDI$ at 3 pm, when $\boldsymbol{m} = 1\%,\ 2\%,\ 3\%,\ 4\%,\ \text{and}\ 5\%$, respectively. According the historical data in Table 1, by using (4), the failure probability for each line length is constant from April to September. Regarding the length of lines, the failure probability moderately increases from October to December, while the failure probability relatively increases from January to March. Thus, only the fragility curve of $FFDI$ at 3 pm is considered in the analyses and simulations of this project. The next section will introduce how to estimate the day-ahead $FFDI$ by using an intelligent-based method.

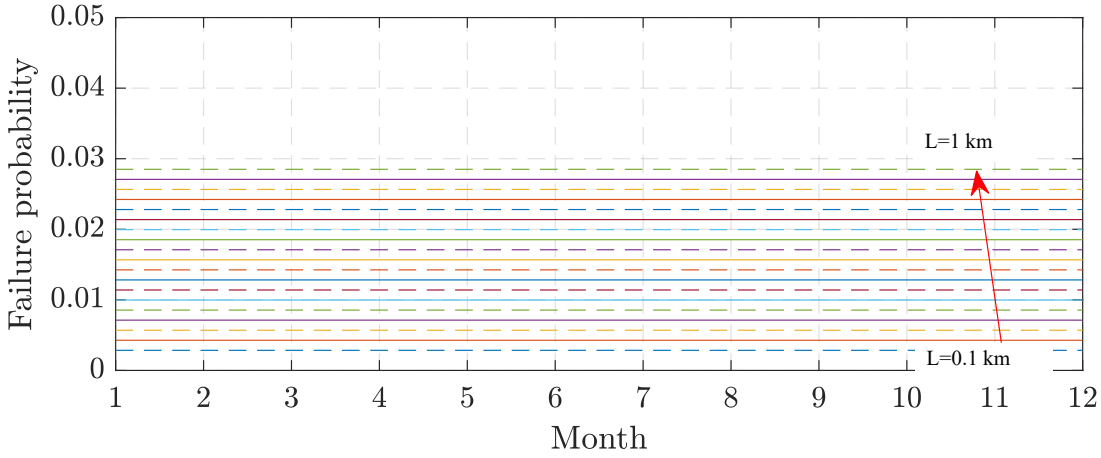

Figure 14: Fragility curve of $FFDI$ at 9 am.

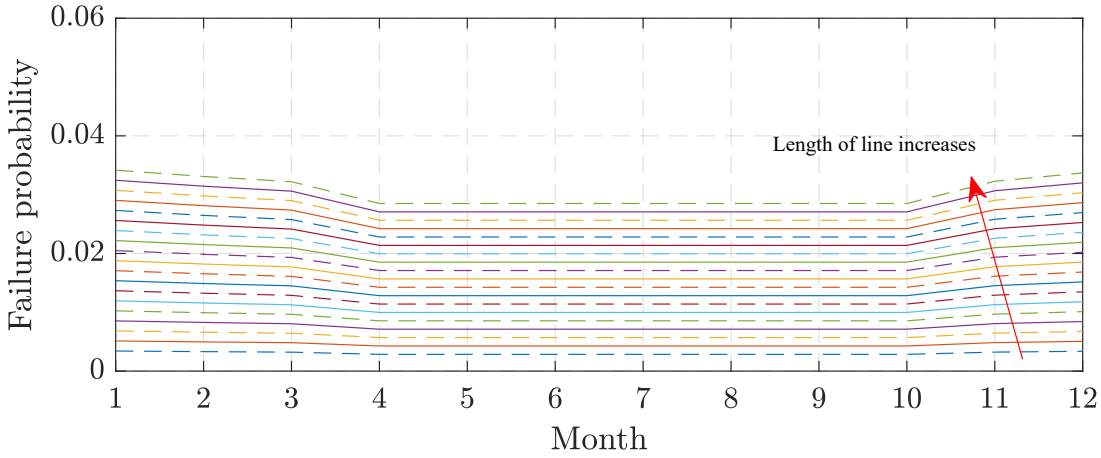

Figure 15: Fragility curve of $FFDI$ at 3 pm (m = 1% (0.01)).

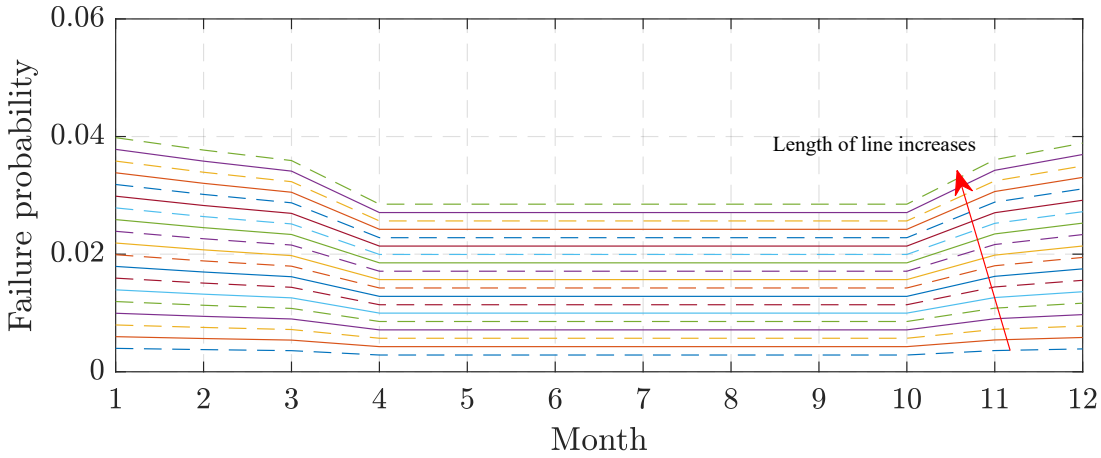

Figure 16: Fragility curve of $FFDI$ at 3 pm (m = 2% (0.02)).

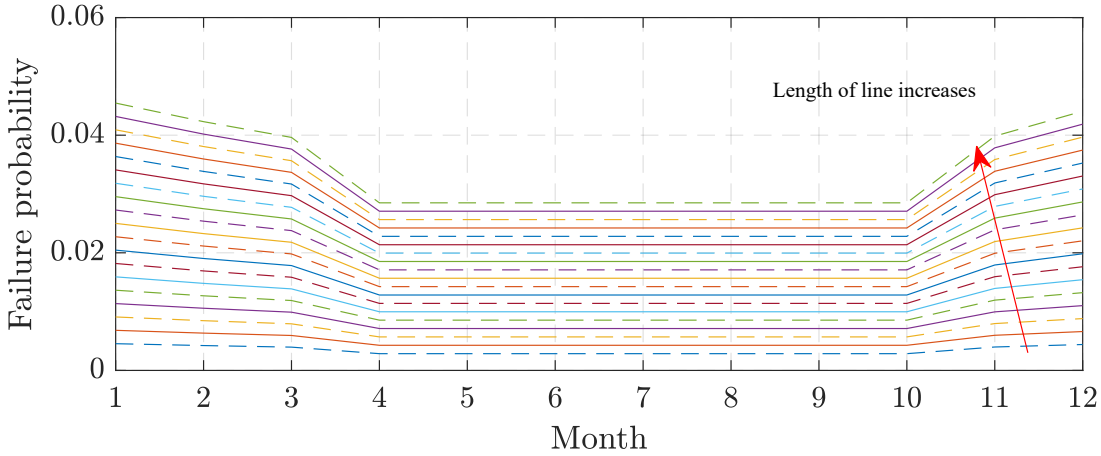

Figure 17: Fragility curve of $FFDI$ at 3 pm (m = 3% (0.03)).

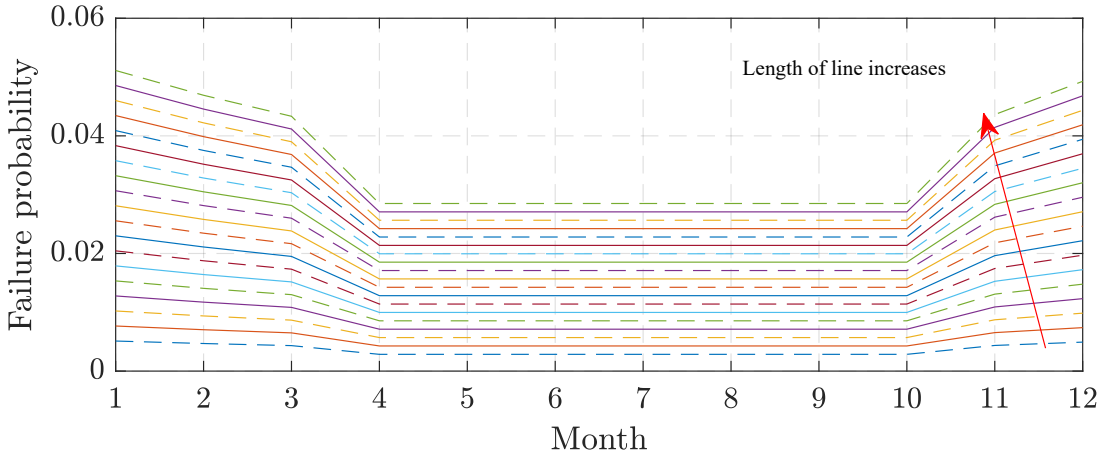

Figure 18: Fragility curve of $FFDI$ at 3 pm (m = 4% (0.04)).

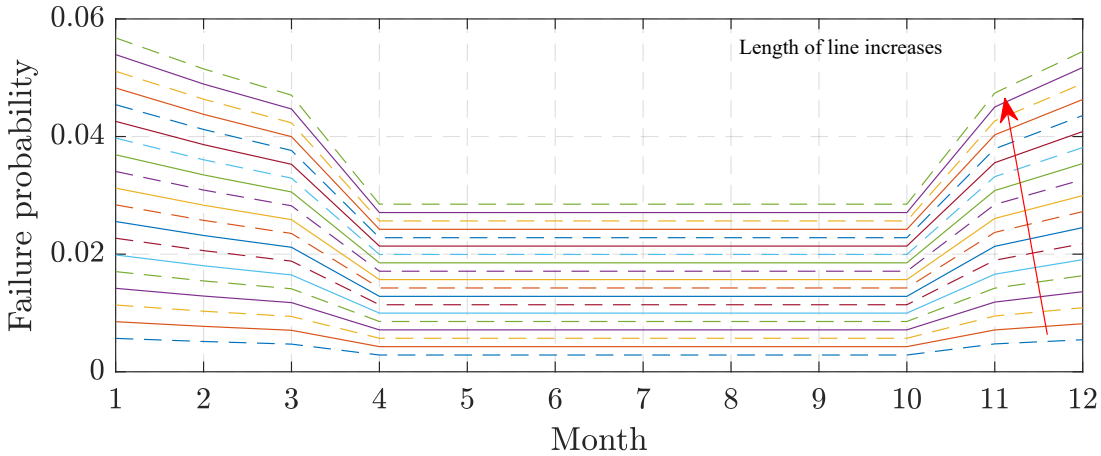

Figure 19: Fragility curve of $FFDI$ at 3 pm (m = 5% (0.05)).

3.4. Parameterizations and Key Indices

From **Project 5**, the value of customer reliability (VCR) for different type and location of the Australian customer can be obtained from the AER (Australian Energy Regulator) reports. The net present cost of value of customer reliability based on the expected energy not supplied (NPC_{VCR}) can be calculated by,

$$NPC_{VCR} = \sum_{i=1}^{n_i} \frac{EENS(t) \times VCR(t)}{(1+d)^i} \quad (5)$$

where t is the time, d is the discounted rate, $i = 1, \dots, n_i$ is the number of years, n_i is the total number of years, and $EENS(t)$ is the expected energy not supplied considering dynamic bushfire.

From **Project 7**, the $FFDI$ is a commonly used metric that indicates the risk of bushfire ignition in different regions in Australia. Several factors are used to calculate the $FFDI$, i.e., intensity of wildfire, gird exposure, grid vulnerability, temperature, windspeed, relative humidity, precipitation level, drought, rainfall. The detail of $FFDI$ can be found in **Project 7**, Section 3.3. The high $FFDI$ can lead to the increment of probability of sub-transmission line failures. For each sub-transmission line $st = 1, \dots, n_{st}$, the probability of failure based on the $FFDI$ ($\mathbf{P}_{FFDI}^{st}$) can be therefore obtained by (4). After matching the $FFDI$ and fragility curve in at each feeder/ transmission line, we can obtain P_{FFDI} for each feeder/ transmission line, thus obtaining $\mathbf{P}_{FFDI}^{st}$ as follows:

$$\mathbf{P}_{FFDI}^{st} = \left[P_{FFDI}^{1}, P_{FFDI}^{2}, \dots, P_{FFDI}^{n_{st}}\right] \quad (6)$$

where $st = 1, \dots, n_{st}$ is the counter of sub-transmission line, and n_{st} is the total number of sub-transmission line.

Next, the probability matrix of supply disruption in day due to dynamic bushfire ($\mathbf{P}_{dd}^{dis}$) is given by,

$$\mathbf{P}_{dd}^{dis} = \left[\mathrm{P}_{dd}^{0-\mathrm{day}}, P_{dd}^{1-\mathrm{day}}, P_{dd}^{2-\mathrm{day}}, \dots, P_{dd}^{n_{dis}-\mathrm{day}}\right] \quad (7)$$

where superscript $dis = 0-\mathrm{day}, 1-\mathrm{day}, \dots, n_{dis}-\mathrm{day}$ represents the number of supply disruption in day, and n_{dis} is the total number of disruption days.

In (4), we have the following constraints:

$$\sum \mathbf{P}_{dd}^{dis} = 1 \quad (8)$$

$$\mathrm{P}_{dd}^{0-\mathrm{day}} > P_{dd}^{1-\mathrm{day}} > P_{dd}^{2-\mathrm{day}} \dots > P_{dd}^{n_{dis}-\mathrm{day}} \quad (9)$$

Note that, according to **Project 7**, assumptions can be made to specify the probabilities of bushfire-induced fuel supply disruption duration.

Next, the vector value of VCR based on (7) ($\mathbf{VCR}_{dd}^{dis}$) is calculated by,

$$\mathbf{VCR}_{dd}^{dis} = \mathbf{VCR}_{0}^{dis} \times \mathbf{P}_{dd}^{dis} \quad (10)$$

or equivalently,

$$\mathbf{VCR}_{dd}^{dis} = \left[VCR_{dd}^{0-\mathrm{day}}, VCR_{dd}^{1-\mathrm{day}}, \dots, VCR_{dd}^{n_{dis}-\mathrm{day}}\right] \quad (11)$$

where $\mathbf{VCR}_{0}^{dis}$ is the updated value of customer reliability depending on several factors such as Consumer Price Index, etc., which is discussed in [5].

3.5. Bushfire Modeling for Reliability Analysis

To consider the dynamic bushfire, the bushfire spreading distance (S_{BF}) can be approximated by,

$$S_{BF} = \beta \bar{V}_w t \quad (12)$$

where $\bar{V}_w$ is the average wind speed, and β is a small number representing the spreading factor of dynamic bushfire. Different values of β can be also investigated in this project. To investigate in more detail, note that S_{BF} can be formulated by other distancing equations, if applicable.

The initial outage matrix of sub-transmission line ($\mathbf{L}_{s}^{st}$) can be obtained by,

$$\mathbf{L}_{s}^{st} = \begin{cases} 0, \text{if } \mathrm{rand}(0\ 1) \leq \mathbf{P}_{FFDI}^{st} \\ 1, \text{if } \mathrm{rand}(0\ 1) > \mathbf{P}_{FFDI}^{st} \end{cases} \quad (13)$$

In (13), logics 0 and 1 respectively represents with and without line outages, $\mathrm{rand}(0\ 1)$ means the random between (0 1). Rewriting (13), for all sub-transmission lines, we have,

$$\mathbf{L}_s^{st} = \left[\mathbf{L}_s^{st,(0-\mathrm{day})}, \mathbf{L}_s^{st,(1-\mathrm{day})}, \dots, \mathbf{L}_s^{st,(n_{dis}-\mathrm{day})}\right]$$
$$\mathbf{L}_s^{st} = \begin{bmatrix} \left[\mathbf{L}_s^{1,(0-day)}, \dots, \mathbf{L}_s^{n_{st},(0-day)}\right] \\ \vdots \\ \left[\mathbf{L}_s^{1,(n_{dis}-day)}, \dots, \mathbf{L}_s^{n_{st},(n_{dis}-day)}\right] \end{bmatrix}^T \tag{14}$$

Let $\mathbf{S}^{(i,j)}$ be the matrix of any distances between lines i and j (obtained from microgrid topology or spatial data) as,

$$\mathbf{S}^{(i,j)} = \left[S^{(1,1)}, S^{(1,2)}, \dots, S^{(n_i n_j)}\right] \tag{15}$$

where $i = 1, \dots, n_i$ and $j = 1, \dots, n_j$ are the corresponding line index.

Considering (6), (12), and (14) after the occurrence of dynamic bushfire, the feeder/transmission line outages of the next consecutive days can be obtained by modifying (6) as:

$$\mathbf{P}_{FFDI}^{st,dis} = \left[\mathbf{P}_{FFDI}^{st,(0-\mathrm{day})}, \mathbf{P}_{FFDI}^{st,(1-\mathrm{day})}, \dots, \mathbf{P}_{FFDI}^{st,(n_{dis}-\mathrm{day})}\right] \tag{16}$$

Then, (16) can be expressed by,

$$\mathbf{P}_{FFDI}^{st,dis} = \begin{bmatrix} \left[P_{FFDI}^{1,(0-\mathrm{day})}, P_{FFDI}^{2,(0-\mathrm{day})}, \dots, P_{FFDI}^{n_{st},(0-\mathrm{day})}\right] \\ \left[P_{FFDI}^{1,(1-\mathrm{day})}, P_{FFDI}^{2,(1-\mathrm{day})}, \dots, P_{FFDI}^{n_{st},(1-\mathrm{day})}\right] \\ \vdots \\ \left[P_{FFDI}^{1,(n_{dis}-\mathrm{day})}, P_{FFDI}^{2,(n_{dis}-\mathrm{day})}, \dots, P_{FFDI}^{n_{st},(n_{dis}-\mathrm{day})}\right] \end{bmatrix}^T \tag{17}$$

Considering (16) and (17), we can find the effects of dynamic bushfire on the supply disruption after the first day of occurrence as follows:

$$\mathbf{P}_{FFDI}^{st,(0-\mathrm{day})} = \left[\mathbf{P}_{FFDI}^{st,(0-\mathrm{day})}\right],$$
$$\mathbf{P}_{FFDI}^{st,(1-\mathrm{day})} = \left[\mathbf{P}_{FFDI}^{st,(0-\mathrm{day})}, \mathbf{P}_{FFDI}^{*,st,(1-\mathrm{day})}\right],$$
$$\mathbf{P}_{FFDI}^{st,(2-\mathrm{day})} = \left[\mathbf{P}_{FFDI}^{st,(1-\mathrm{day})}, \mathbf{P}_{FFDI}^{*,st,(2-\mathrm{day})}\right],\dots$$
$$\dots,\mathbf{P}_{FFDI}^{st(n_{dis}-\mathrm{day})} = \left[\mathbf{P}_{FFDI}^{st,(n_{dis}-\mathrm{day}-1)}, \mathbf{P}_{FFDI}^{*,st,(n_{dis}-\mathrm{day})}\right] \tag{18}$$

From (14), let *i)* $\mathbf{L}_s^{st,(1-\mathrm{day})}, \mathbf{L}_s^{st,(2-\mathrm{day})}, \dots, \mathbf{L}_s^{st,(n_{dis}-\mathrm{day})}$ respectively be the line status matrices after $1-\mathrm{day}$, $2-\mathrm{day}$, …, $n_{dis}-\mathrm{day}$ of the occurrence of dynamic bushfire, and *ii)* $\mathbf{S}^{(i,j),(1-\mathrm{day})}, \mathbf{S}^{(i,j),(2-\mathrm{day})}, \dots, \mathbf{S}^{(i,j),(n_{dis}-\mathrm{day})}$ respectively be matrices of distances between any corresponding lines after $1-\mathrm{day}$, $2-\mathrm{day}$, …, $n_{dis}-\mathrm{day}$ of the occurrence of dynamic bushfire. Matrices $\mathbf{P}_{FFDI}^{*,st,(1-\mathrm{day})}, \dots, \mathbf{P}_{FFDI}^{*,st,(n_{dis}-\mathrm{day})}$ in (15) can be found by the following equations:

$$\mathbf{P}_{FFDI}^{*,st,(1-\mathrm{day})} = \mathbf{L}_s^{st,(1-\mathrm{day})} = \begin{cases} 0, \text{if } \mathbf{S}^{(i,j),(1-\mathrm{day})} < \alpha \bar{V}_w t \\ 1, \text{if } \mathbf{S}^{(i,j),(1-\mathrm{day})} \geq \alpha \bar{V}_w t \end{cases},$$
$$\mathbf{P}_{FFDI}^{*,st,(2-\mathrm{day})} = \mathbf{L}_s^{st,(2-\mathrm{day})} = \begin{cases} 0, \text{if } \mathbf{S}^{(i,j),(1-\mathrm{day})} < 2\alpha \bar{V}_w t \\ 1, \text{if } \mathbf{S}^{(i,j),(1-\mathrm{day})} \geq 2\alpha \bar{V}_w t \end{cases},\dots$$
$$\dots,\mathbf{P}_{FFDI}^{*,st,(n_{dis}-\mathrm{day})} = \mathbf{L}_s^{st,(n_{dis}-\mathrm{day})} = \begin{cases} 0, \text{if } \mathbf{S}^{(i,j),(n_{dis}-\mathrm{day})} < n_{dis}\alpha \bar{V}_w t \\ 1, \text{if } \mathbf{S}^{(i,j),(n_{dis}-\mathrm{day})} \geq n_{dis}\alpha \bar{V}_w t \end{cases} \tag{19}$$

By substituting (19) into (18), we get the line status matrices due to consecutive effects of the bushfire in $1-\mathrm{day}$, $2-\mathrm{day}$, …, $n_{dis}-\mathrm{day}$. Therefore, the $EENS$ in (1) affected by the dynamic bushfire ($EENS(t)$) are obtained as,

$$EENS(t) = \left[EENS^{(0-\text{day})}, EENS^{(1-\text{day})}, \dots, EENS^{(n_{dis}-\text{day})}\right] \quad (20)$$

Finally, the total NPC_{VCR} under the effects of dynamic bushfire (NPC_{VCR}^{tot}) can be calculated by,

$$NPC_{VCR}^{tot} = \sum\left(\mathbf{P}_{dd}^{dis} * \mathbf{NPC}_{VCR}(\mathbf{VCR}_{dd}^{dis})\right) \quad (21)$$

When the $\mathbf{NPC}_{VCR}$ is a function of the $\mathbf{VCR}_{dd}^{dis}$, where $\mathbf{VCR}_{dd}^{dis}$ is calculated by,

$$\mathbf{VCR}_{dd}^{dis} = f\left(dis, \mathbf{P}_{dd}^{dis}, \dots\right) = \mathbf{VCR}_{dd}^{initial}\left[1 + \left(\mathbf{P}_{dd}^{dis} \times e^{\frac{dis}{\sigma}}\right)\right] \quad (22)$$

$$\mathbf{VCR}_{dd}^{dis} = \left[VCR_{dd}^{0-\text{day}}, VCR_{dd}^{1-\text{day}}, \dots, VCR_{dd}^{n_{dis}-\text{day}}\right] \quad (23)$$

From (23), the following constraint is found,

$$VCR_{dd}^{0-\text{day}} < VCR_{dd}^{1-\text{day}} < \cdots \ll VCR_{dd}^{n_{dis}-\text{day}} \quad (24)$$

where $\mathbf{VCR}_{dd}^{initial}$ is the updated VCR, and σ is the divided factor in which $f\left(dis, \mathbf{P}_{dd}^{dis}, \dots\right)$ can be represented by a linear, a nonlinear, or an exponential function of dis and $\mathbf{P}_{dd}^{dis}$.

To consider different types of loads, i.e., residential, commercial, and industrial loads, the $\mathbf{VCR}_{dd}^{initial}$ is expressed by,

$$\mathbf{VCR}_{dd}^{initial} = \left[VCR_{dd}^{initial,res}\ VCR_{dd}^{initial,com}\ VCR_{dd}^{initial,ind}\right] \quad (25)$$

where superscripts res, com, and ind mean belonging to the residential, commercial, and industrial loads, respectively.

By substituting (25) into (22), (21) can be expressed by considering the ratio of each load type as,

$$NPC_{VCR}^{tot} = \frac{S_L^{res}}{S_L^{tot}} NPC_{VCR}^{tot,res} + \frac{S_L^{com}}{S_L^{tot}} NPC_{VCR}^{tot,com} + \frac{S_L^{ind}}{S_L^{tot}} NPC_{VCR}^{tot,ind} \quad (26)$$

where S_L^{tot} is the total of load consumptions obtained by,

$$S_L^{tot} = S_L^{res} + S_L^{com} + S_L^{ind} \quad (27)$$

When $NPC_{VCR}^{tot,res}$, $NPC_{VCR}^{tot,com}$, and $NPC_{VCR}^{tot,ind}$ are calculated by,

$$NPC_{VCR}^{tot,res} = \left(\mathrm{P}_{dd}^{0-\text{day}} \times \sum_{i=1}^{n_i} \frac{EENS^{(0-\text{day})} \times VCR_{dd}^{(0-\text{day}),res}}{(1+d)^i}\right) + \left(\mathrm{P}_{dd}^{1-\text{day}} \times \sum_{i=1}^{n_i} \frac{EENS^{(1-\text{day})} \times VCR_{dd}^{(1-\text{day}),res}}{(1+d)^i}\right) + \cdots + \left(\mathrm{P}_{dd}^{n_{dis}-\text{day}} \times \sum_{i=1}^{n_i} \frac{EENS^{(n_{dis}-\text{day})} \times VCR_{dd}^{(n_{dis}-\text{day}),res}}{(1+d)^i}\right) \quad (28)$$

$$NPC_{VCR}^{tot,com} = \left(\mathrm{P}_{dd}^{0-\text{day}} \times \sum_{i=1}^{n_i} \frac{EENS^{(0-\text{day})} \times VCR_{dd}^{(0-\text{day}),com}}{(1+d)^i}\right) + \left(\mathrm{P}_{dd}^{1-\text{day}} \times \sum_{i=1}^{n_i} \frac{EENS^{(1-\text{day})} \times VCR_{dd}^{(1-\text{day}),com}}{(1+d)^i}\right) + \cdots + \left(\mathrm{P}_{dd}^{n_{dis}-\text{day}} \times \sum_{i=1}^{n_i} \frac{EENS^{(n_{dis}-\text{day})} \times VCR_{dd}^{(n_{dis}-\text{day}),com}}{(1+d)^i}\right) \quad (29)$$

$$NPC_{VCR}^{tot,ind} = \left(\mathrm{P}_{dd}^{0-\text{day}} \times \sum_{i=1}^{n_i} \frac{EENS^{(0-\text{day})} \times VCR_{dd}^{(0-\text{day}),ind}}{(1+d)^i}\right) + \left(\mathrm{P}_{dd}^{1-\text{day}} \times \sum_{i=1}^{n_i} \frac{EENS^{(1-\text{day})} \times VCR_{dd}^{(1-\text{day}),ind}}{(1+d)^i}\right) + \cdots + \left(\mathrm{P}_{dd}^{n_{dis}-\text{day}} \times \sum_{i=1}^{n_i} \frac{EENS^{(n_{dis}-\text{day})} \times VCR_{dd}^{(n_{dis}-\text{day}),ind}}{(1+d)^i}\right) \quad (30)$$

3.6. Conceptual Framework

The flowchart to evaluate bushfire effects on the reliability of Donald and Tarnagulla microgrids is demonstrated in Figure 20. In this project, DIgSILENT PowerFactory and MATLAB are employed for the analysis of value of customer reliability considering the dynamic bushfire in which the interface of these programs is shown in Figure 21. It is worth nothing that, if applicable, other related programs or

tools can be incorporated in the framework for future reliability analysis of the Donald and Tarnagulla networks.

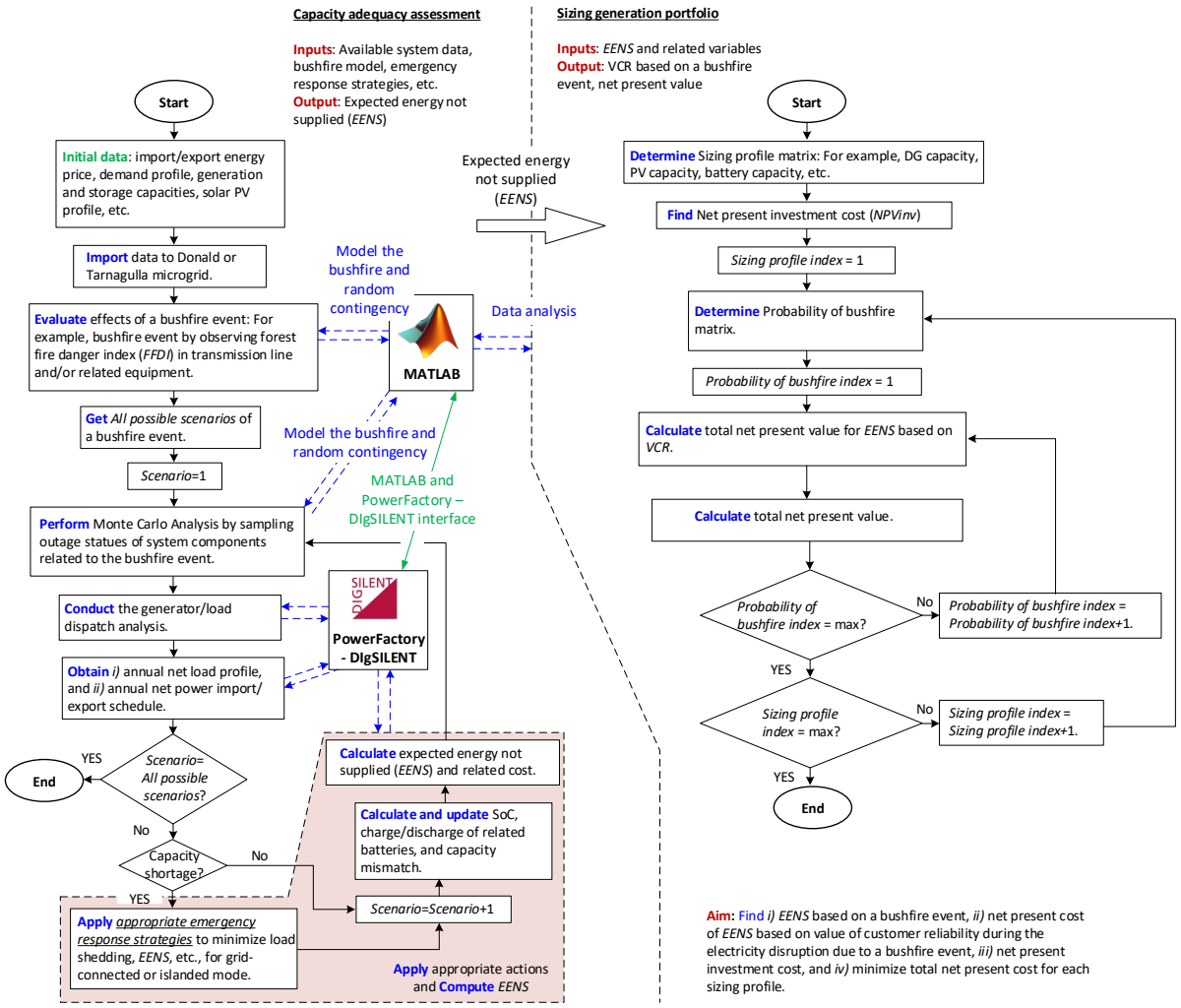

Figure 20: Flowchart of the reliability assessment considering dynamic bushfire.

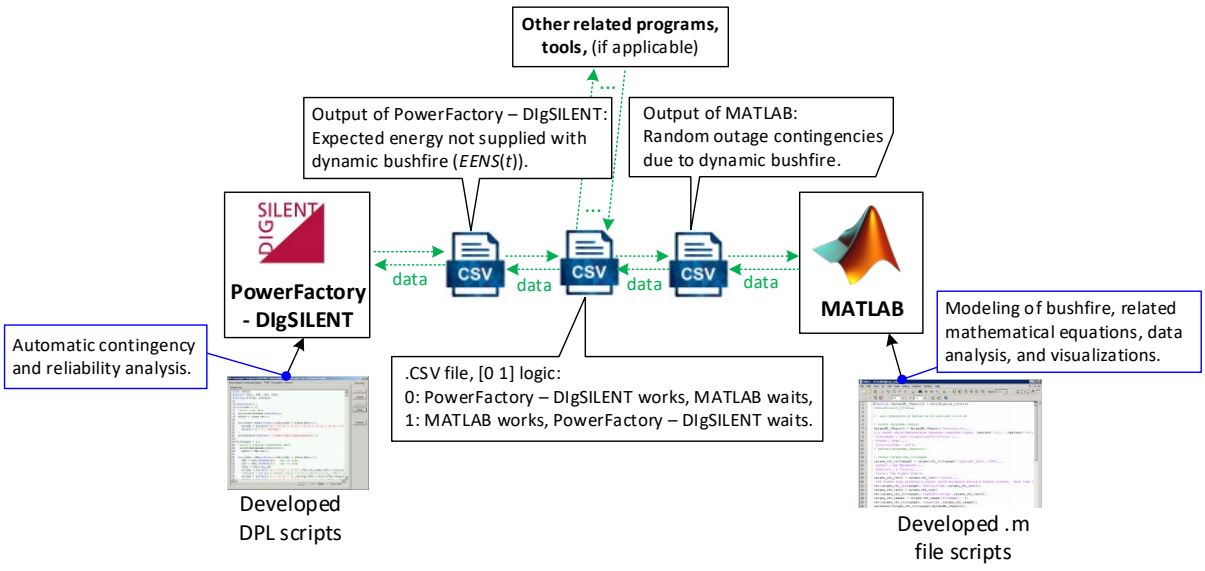

Figure 21: MATLAB and PowerFactory – DIgSILENT interface.

4. Effects of Bushfire on Reliability in Worst Scenario

4.1. Results in the Tarnagulla Network

The Tarnagulla network is used to test the process developed in prior section. The required generation capacity for Tarnagulla area is adopted from the sizing results of **Project 5 and Project 7**. However, in the worst scenario, two assumptions are additionally assumed as follows: *i)* there are no emergency response from the batteries, and *ii)* the powers supported from solar photovoltaic (SPV) generations are unavailable to support the load due to worst climate situation. Next, three different factors related to the dynamic bushfire are altered as follows: *i)* duration of supply disruption due to the bushfire dynamic are varied from 0.5 to 10 days (i.e., $dis = \frac{1}{2} - day, 1 - day, 1\frac{1}{2} - day, \dots, 10 - day$); Note that since the spreading rate of bushfire is considered, this duration can be observed in a smaller step which will be presented in the next report. Different from previous reports, thus the $EENS$ is varied according to time-domain as demonstrated in (), *ii)* the spreading factor of dynamic bushfire is regarded by $\beta = 0.01, 0.02, \dots, 0.05$, and *iii)* the sensitivity of feeder/transmission line failure rates is considered by $\boldsymbol{m} = 1\%,\ 3\%,\ \text{and}\ 5\%$.

The sensitivity analyses of $EENS$ regarding the mentioned factors are illustrated in Figure 22. The obtained result demonstrates that *i)* when $\boldsymbol{m}$ increases, this scenario results in the increment of failure probability, and *ii)* when the duration of supply disruption increases, the $EENS$ relatively increases according to the supply disruption duration due to the bushfire dynamics.

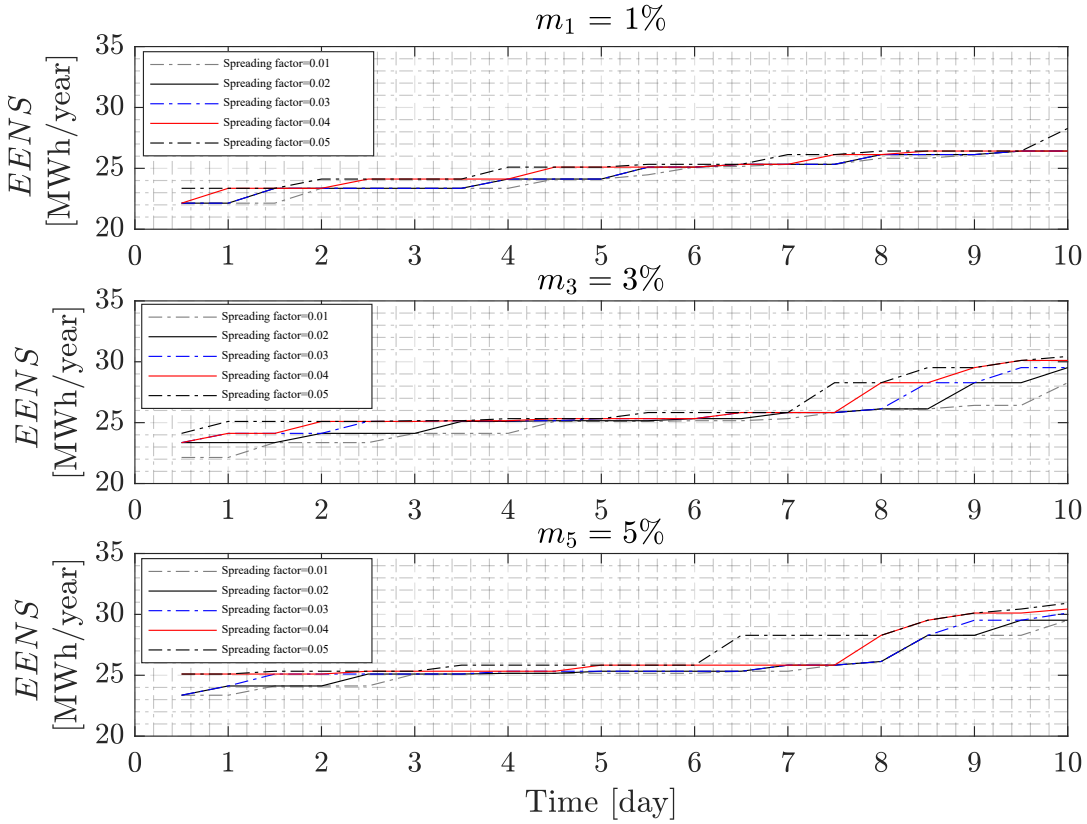

Figure 22: Results of $EENS$ considering bushfire of Tarnagulla network under different values of $\boldsymbol{m}$ and β.

To compute the value of customer affected by the dynamic bushfire, the updated VCR for 2021 is 22.58 AU$/kWh according to [5], i.e., $\mathbf{VCR}_{dd}^{initial} = 22.58$. Here, the probability sets are assumed for 50 different

scenarios, i.e., $\mathbf{P}_{dd}^{dis} = \mathrm{sort}\left(\mathrm{rand}\left(50, \mathrm{length}(dis)\right)\right)$, where $\sum \mathbf{P}_{dd}^{dis} = 1$, sort represents sorting the element in ascending order, $\mathrm{rand}(i,j)$ means to random a matrix with i row and j column, and length is the length of matrix or vector. Table 3 shows the different 50 probability sets used in this study. By using mathematical equations of the dynamic bushfire described in **Sections 3.5** and **3.6**, and $\sigma = 5$, Figure 24 shows the value of customer reliability, i.e., NPC_{VCR}, considering the dynamic bushfire under different 50 probability sets. The values of NPC_{VCR}^{tot} are calculated by (26). The mean values of NPC_{VCR}^{tot} ($\overline{NPC}_{VCR}^{tot} = \frac{NPC_{VCR}^{tot,1} + NPC_{VCR}^{tot,2} + \cdots + NPC_{VCR}^{tot,50}}{50}$) are also given. It is seen that the $\overline{NPC}_{VCR}^{tot}$ increase when $\boldsymbol{m}$ increases. By simulation with various probability conditions, the upper and lower boundaries for the worst scenario can be observed for the value of customer reliability under effects of the dynamic bushfire.

Table 2 Random probability sets

	Random probability sets [scenario 1 to scenario 10]									
dis=0.5	0.095006	0.094307	0.08123	0.115223	0.08583	0.100731	0.075584	0.126402	0.095745	0.084114
dis =1.0	0.090085	0.090616	0.080807	0.10482	0.084121	0.100121	0.073459	0.106656	0.083924	0.079965
dis =1.5	0.089906	0.089502	0.08031	0.100418	0.081182	0.091586	0.072527	0.100899	0.082573	0.079623
dis =2.0	0.080346	0.086884	0.079428	0.097402	0.075338	0.088398	0.065825	0.099432	0.081117	0.078707
dis =2.5	0.080015	0.084365	0.072798	0.096308	0.072486	0.075104	0.065644	0.085645	0.080673	0.069341
dis =3.0	0.07961	0.076079	0.066895	0.078242	0.071037	0.071556	0.059236	0.077439	0.0781	0.06794
dis =3.5	0.071398	0.075892	0.066356	0.073152	0.064447	0.068211	0.058785	0.076215	0.072555	0.067923
dis =4.0	0.065904	0.062537	0.065925	0.057636	0.063393	0.06573	0.058725	0.075407	0.056254	0.065965
dis =4.5	0.0642	0.049997	0.060261	0.05429	0.063276	0.061209	0.052234	0.073751	0.055606	0.057823
dis =5.0	0.051882	0.049782	0.056788	0.052945	0.057511	0.057869	0.044841	0.06543	0.043591	0.05058
dis =5.5	0.047994	0.044649	0.05	0.040561	0.053453	0.040743	0.044677	0.022279	0.042907	0.049833
dis =6.0	0.047593	0.044133	0.04881	0.033252	0.049194	0.03935	0.043979	0.015337	0.040914	0.047386
dis =6.5	0.037427	0.04145	0.045069	0.025547	0.042722	0.039293	0.041309	0.013078	0.033687	0.044524
dis =7.0	0.028229	0.033881	0.040793	0.015967	0.041548	0.027778	0.041155	0.011401	0.031965	0.038015
dis =7.5	0.026632	0.027408	0.03325	0.015631	0.020132	0.018495	0.041108	0.011121	0.031621	0.037988
dis =8.0	0.020658	0.02484	0.028793	0.011051	0.018291	0.017064	0.038645	0.010725	0.022915	0.037929
dis =8.5	0.008997	0.013691	0.023252	0.008917	0.016758	0.01276	0.036905	0.010575	0.021995	0.020019
dis =9.0	0.008506	0.006879	0.014309	0.007947	0.01603	0.012748	0.032426	0.009918	0.017847	0.016535
dis =9.5	0.004346	0.002841	0.004011	0.005693	0.012129	0.008615	0.028517	0.004819	0.014885	0.003314
dis =10.0	0.001265	0.000265	0.000914	0.004996	0.011121	0.00264	0.024418	0.003471	0.011125	0.002477

Table 3 Random probability sets (cont.)

	Random probability sets [scenario 11 to scenario 20]									
dis *=0.5*	0.101037	0.074427	0.083389	0.102126	0.106374	0.088791	0.088866	0.114878	0.118701	0.108363
dis *=1.0*	0.098774	0.07338	0.082617	0.091644	0.099538	0.088093	0.088618	0.106081	0.103535	0.093609
dis *=1.5*	0.096246	0.068038	0.082563	0.090733	0.092445	0.08427	0.082211	0.103631	0.102457	0.09328
dis *=2.0*	0.089874	0.063112	0.082512	0.089758	0.087996	0.075685	0.082136	0.101504	0.09178	0.087054
dis *=2.5*	0.086385	0.060626	0.080441	0.068138	0.080571	0.068627	0.074609	0.082936	0.086267	0.084499
dis *=3.0*	0.084659	0.058199	0.075076	0.062146	0.075369	0.066056	0.066792	0.079757	0.081816	0.07928
dis *=3.5*	0.066262	0.057015	0.073886	0.060149	0.068353	0.064711	0.064885	0.068503	0.079987	0.072868
dis *=4.0*	0.064782	0.055906	0.069683	0.055458	0.061034	0.06456	0.062151	0.06129	0.052871	0.066391
dis *=4.5*	0.064734	0.055618	0.062622	0.053974	0.060492	0.056524	0.058554	0.058695	0.043789	0.063686

dis =5.0	0.062783	0.054667	0.058302	0.050844	0.055781	0.05489	0.050185	0.043565	0.041174	0.045545
dis =5.5	0.048434	0.052847	0.043518	0.04682	0.046321	0.053576	0.047602	0.040476	0.039328	0.039934
dis =6.0	0.033925	0.051807	0.040382	0.04094	0.037548	0.044751	0.046787	0.035737	0.034336	0.039161
dis =6.5	0.027238	0.048658	0.039217	0.034167	0.035798	0.043522	0.033618	0.030494	0.027391	0.036081
dis =7.0	0.017566	0.045865	0.038109	0.031433	0.034453	0.030277	0.030272	0.018293	0.025567	0.024925
dis =7.5	0.01496	0.041649	0.036238	0.027039	0.017354	0.029277	0.030219	0.013834	0.022345	0.024764
dis =8.0	0.014182	0.040013	0.013798	0.022944	0.015874	0.026033	0.026605	0.013567	0.019254	0.014426
dis =8.5	0.01353	0.035413	0.013435	0.022747	0.012242	0.018985	0.023519	0.011367	0.017119	0.010717
dis =9.0	0.008598	0.033318	0.012452	0.020749	0.005596	0.016179	0.021617	0.01049	0.006872	0.008285
dis =9.5	0.003149	0.017861	0.007117	0.015908	0.005209	0.013411	0.014124	0.002548	0.005087	0.003647
dis =10.0	0.002884	0.011581	0.004642	0.012283	0.001653	0.011783	0.006629	0.002354	0.000325	0.003486

Table 4 Random probability sets (cont.)

	Random probability sets [scenario 21 to scenario 30]									
dis =0.5	0.097704	0.103003	0.09553	0.100025	0.109539	0.118768	0.103878	0.093662	0.083647	0.095214
dis =1.0	0.083145	0.102978	0.094175	0.096492	0.085627	0.109181	0.103474	0.085619	0.077046	0.085311
dis =1.5	0.077971	0.098766	0.085598	0.093715	0.081352	0.097211	0.088968	0.084962	0.074105	0.085144
dis =2.0	0.076166	0.094648	0.082504	0.078863	0.076896	0.085549	0.082848	0.081779	0.068007	0.076235
dis =2.5	0.075015	0.085573	0.070306	0.072118	0.068324	0.066246	0.077018	0.070586	0.067458	0.072591
dis =3.0	0.06655	0.082176	0.069604	0.066685	0.065829	0.062612	0.059016	0.070499	0.06742	0.065929
dis =3.5	0.062953	0.075255	0.068542	0.05935	0.064966	0.061552	0.057537	0.065599	0.066572	0.065842
dis =4.0	0.058898	0.06447	0.067251	0.05652	0.053737	0.058308	0.05434	0.065062	0.064221	0.053954
dis =4.5	0.056312	0.052065	0.06352	0.055417	0.050778	0.057074	0.051415	0.064948	0.061279	0.047249
dis =5.0	0.048717	0.036521	0.041754	0.049272	0.048917	0.055012	0.047414	0.056286	0.056802	0.046263
dis =5.5	0.046607	0.035237	0.038799	0.047244	0.044518	0.054982	0.04501	0.050809	0.054998	0.045612
dis =6.0	0.04035	0.032906	0.03586	0.046645	0.043611	0.054545	0.03878	0.035494	0.049266	0.043829
dis =6.5	0.040224	0.03176	0.031878	0.041777	0.039145	0.035103	0.035116	0.028986	0.042433	0.043493
dis =7.0	0.037734	0.031446	0.030496	0.032835	0.032399	0.024148	0.031332	0.025475	0.037157	0.042254
dis =7.5	0.036533	0.02786	0.027194	0.031265	0.031842	0.016861	0.030793	0.022812	0.036146	0.039378
dis =8.0	0.031495	0.018622	0.02658	0.028599	0.031739	0.015466	0.030753	0.021818	0.026843	0.029171
dis =8.5	0.025591	0.015677	0.025409	0.026533	0.029003	0.010829	0.024881	0.020784	0.025626	0.023849
dis =9.0	0.018404	0.007509	0.021061	0.007705	0.016278	0.009889	0.016354	0.01876	0.014382	0.020891
dis =9.5	0.012624	0.002377	0.017997	0.007119	0.013156	0.00453	0.011081	0.018731	0.014262	0.016493
dis =10.0	0.007007	0.001151	0.005941	0.001824	0.012346	0.002132	0.009992	0.017331	0.012331	0.001297

Table 5 Random probability sets (cont.)

	Random probability sets [scenario 31 to scenario 40]									
dis =0.5	0.121584	0.093921	0.106585	0.100357	0.09017	0.086532	0.100669	0.082192	0.095785	0.135812
dis =1.0	0.11077	0.088991	0.097659	0.092009	0.076839	0.085001	0.09656	0.081917	0.094266	0.135497
dis =1.5	0.106127	0.087516	0.097017	0.084537	0.072969	0.084639	0.081756	0.074739	0.083827	0.133013
dis =2.0	0.085447	0.083222	0.083124	0.07796	0.069067	0.079791	0.078655	0.074624	0.078465	0.093015
dis =2.5	0.084158	0.077682	0.082207	0.077427	0.065938	0.07702	0.072821	0.073816	0.073574	0.077422
dis =3.0	0.061445	0.075969	0.072777	0.074163	0.063935	0.074031	0.072592	0.068704	0.072412	0.074163

dis =3.5	0.058156	0.073949	0.068202	0.071726	0.061398	0.073711	0.072563	0.06778	0.064827	0.051514
dis =4.0	0.054825	0.071567	0.066909	0.068755	0.060195	0.072651	0.070903	0.06128	0.060358	0.046008
dis =4.5	0.046504	0.05235	0.060038	0.063251	0.057901	0.066439	0.069594	0.061133	0.047024	0.039253
dis =5.0	0.041412	0.050633	0.051916	0.053347	0.057811	0.061369	0.069254	0.055839	0.045726	0.038335
dis =5.5	0.038504	0.04487	0.046261	0.047489	0.056838	0.057447	0.05456	0.052083	0.042621	0.031198
dis =6.0	0.038192	0.042733	0.041248	0.036997	0.048564	0.049583	0.049551	0.045319	0.04208	0.028599
dis =6.5	0.037731	0.03329	0.034966	0.035758	0.036665	0.032696	0.02569	0.044343	0.033843	0.026519
dis =7.0	0.029917	0.030017	0.027772	0.031541	0.033279	0.02974	0.021953	0.042634	0.032602	0.024919
dis =7.5	0.02748	0.029169	0.021255	0.020406	0.032847	0.027746	0.018402	0.042201	0.031829	0.019767
dis =8.0	0.020925	0.027368	0.018648	0.018807	0.029635	0.015652	0.017715	0.031412	0.028945	0.019224
dis =8.5	0.011283	0.016573	0.012718	0.018377	0.026656	0.012927	0.010068	0.023826	0.027313	0.012368
dis =9.0	0.011221	0.010241	0.005146	0.015864	0.022607	0.011694	0.006516	0.010647	0.024664	0.006715
dis =9.5	0.010863	0.009587	0.003147	0.007938	0.021893	0.001273	0.005985	0.00309	0.019129	0.004044
dis =10.0	0.003457	0.000352	0.002405	0.003293	0.014791	5.84E-05	0.004195	0.002421	0.00071	0.002615

Table 6 Random probability sets (cont.)

	Random probability sets [scenario 41 to scenario 50]									
dis =0.5	0.088954	0.085162	0.090586	0.101832	0.105718	0.099369	0.082176	0.10126	0.112585	0.087604
dis =1.0	0.083698	0.083291	0.087214	0.091697	0.10481	0.098748	0.08059	0.09391	0.111873	0.081828
dis =1.5	0.078775	0.073324	0.080276	0.089974	0.091946	0.088026	0.079979	0.092297	0.094366	0.080474
dis =2.0	0.074632	0.072024	0.077117	0.089644	0.087191	0.086061	0.079223	0.085999	0.092095	0.074689
dis =2.5	0.074621	0.066232	0.076974	0.086587	0.082744	0.073087	0.073051	0.080441	0.077315	0.073456
dis =3.0	0.074428	0.064482	0.075821	0.083156	0.071545	0.071425	0.072353	0.074474	0.074529	0.072961
dis =3.5	0.070365	0.063509	0.061007	0.069942	0.059541	0.062203	0.069635	0.0582	0.068265	0.072598
dis =4.0	0.066865	0.060302	0.058311	0.066917	0.055436	0.059646	0.06582	0.055777	0.068152	0.072193
dis =4.5	0.065426	0.05698	0.053635	0.063826	0.051875	0.050988	0.065371	0.052761	0.065603	0.072179
dis =5.0	0.053557	0.056106	0.049011	0.061064	0.048523	0.050251	0.056625	0.050082	0.05654	0.062172
dis =5.5	0.044556	0.055595	0.045207	0.04515	0.04705	0.04309	0.046429	0.044398	0.037345	0.056676
dis =6.0	0.043295	0.047441	0.043468	0.0393	0.040914	0.041557	0.045412	0.035161	0.035539	0.038195
dis =6.5	0.042021	0.042046	0.04104	0.031547	0.030978	0.037826	0.035266	0.033849	0.029925	0.027128
dis =7.0	0.039884	0.040969	0.038513	0.025128	0.025369	0.037752	0.034739	0.032955	0.022673	0.024727
dis =7.5	0.031932	0.033207	0.034639	0.019062	0.023952	0.02754	0.024701	0.029202	0.021972	0.023699
dis =8.0	0.025408	0.02919	0.029164	0.015388	0.021946	0.024132	0.023846	0.027391	0.011238	0.021648
dis =8.5	0.015406	0.027157	0.027141	0.010691	0.020399	0.018682	0.022145	0.021721	0.006875	0.019065
dis =9.0	0.015154	0.021746	0.013472	0.004884	0.016872	0.017579	0.02065	0.019019	0.005283	0.016954
dis =9.5	0.007635	0.010863	0.013292	0.002126	0.012447	0.009979	0.019702	0.010044	0.004066	0.016758
dis =10.0	0.003388	0.010375	0.004112	0.002085	0.000744	2.06E-03	0.002285	0.001059	0.00376	0.004997

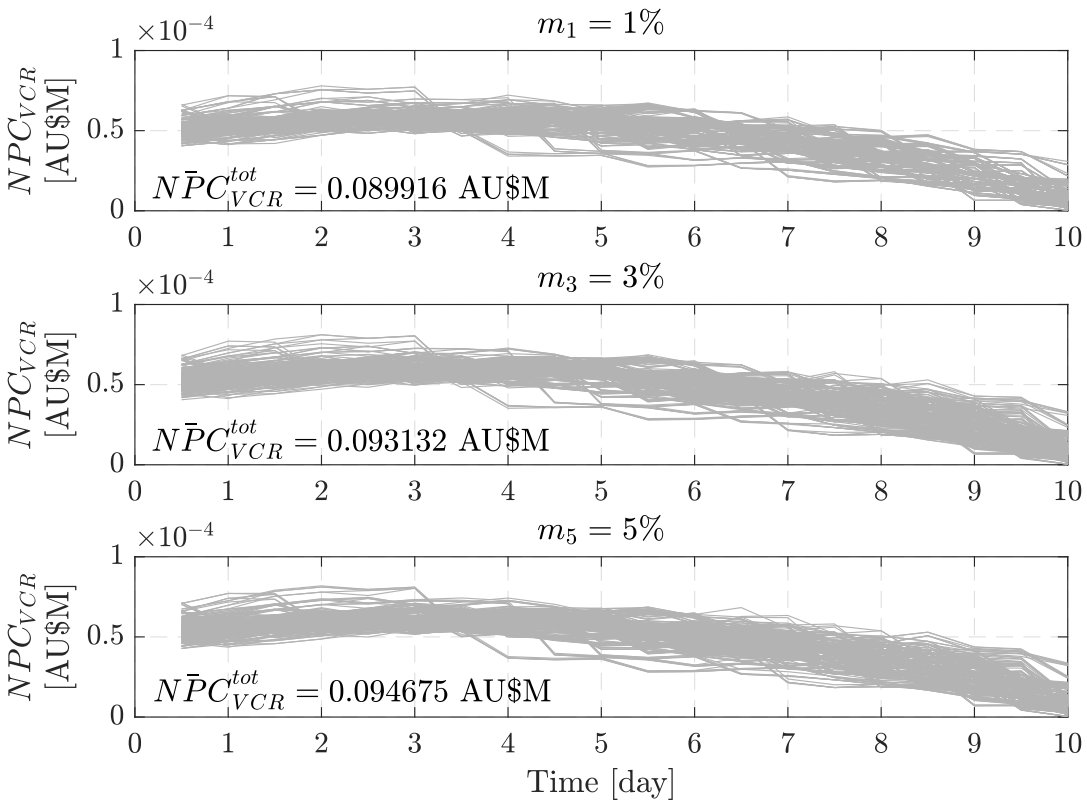

Figure 23: Results of NPC^{tot}_{VCR} considering dynamic bushfire for 50 possible scenarios of Tarnagulla network.

Next, it is assumed that approximately 20%, 40%, 60%, and 80% power outputs from SPVs (assumed by relatively decreasing the sizes of SPVs) are available to supply the loads, while the rests are affected due to the smoke and high temperature. One probability scenario is conducted as given in Table III (in column with green highlights). Here, the values of $\boldsymbol{m} = 5\%$ and $\beta = 5\%$ are regarded. Figures 24, 25, and 26 demonstrate the values of $EENS$, individual NPV_{VCR}, and NPC^{tot}_{VCR} in grid-connected Tarnagulla network, respectively. Figures 27, 28, and 29 show the values of $EENS$, individual NPV_{VCR}, and NPC^{tot}_{VCR} in off-grid Tarnagulla network, respectively. In comparison, all the values of of $EENS$, individual NPV_{VCR}, and NPC^{tot}_{VCR} are relatively smaller in the grid-connected scenario due to higher $EENS$.

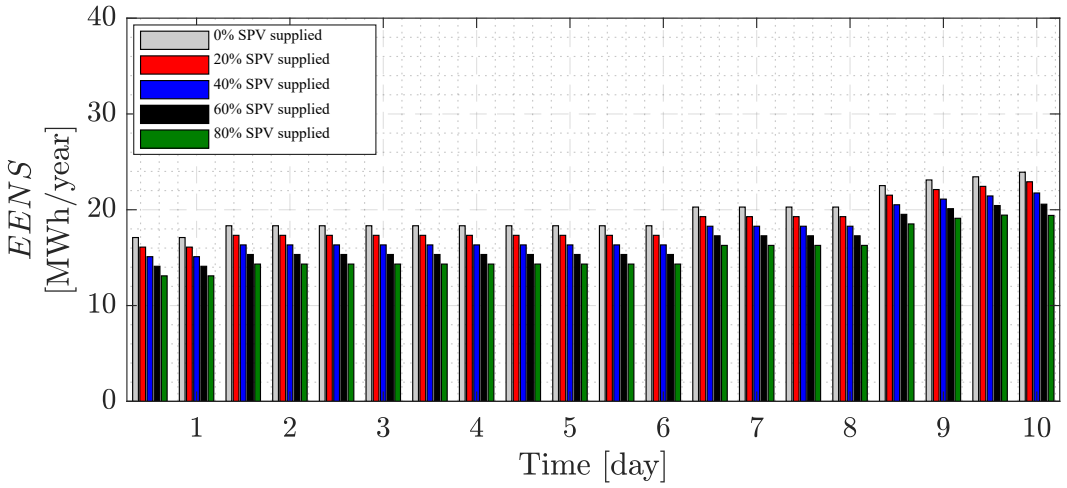

Figure 24: Results of $EENS$ during bushfire in grid-connected scenario of Tarnagulla network.

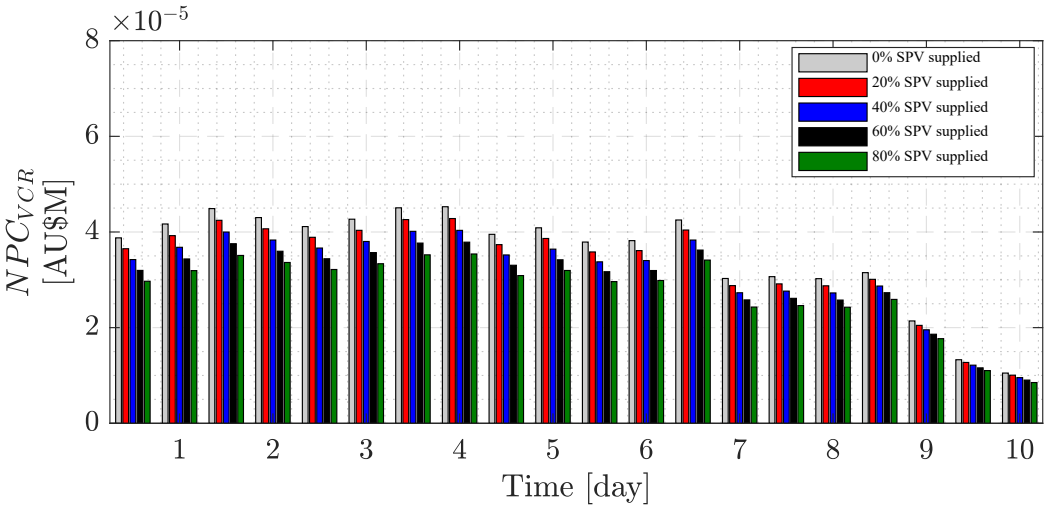

Figure 25: Results of NPV_{VCR} in each day during bushfire in grid-connected scenario of Tarnagulla network.

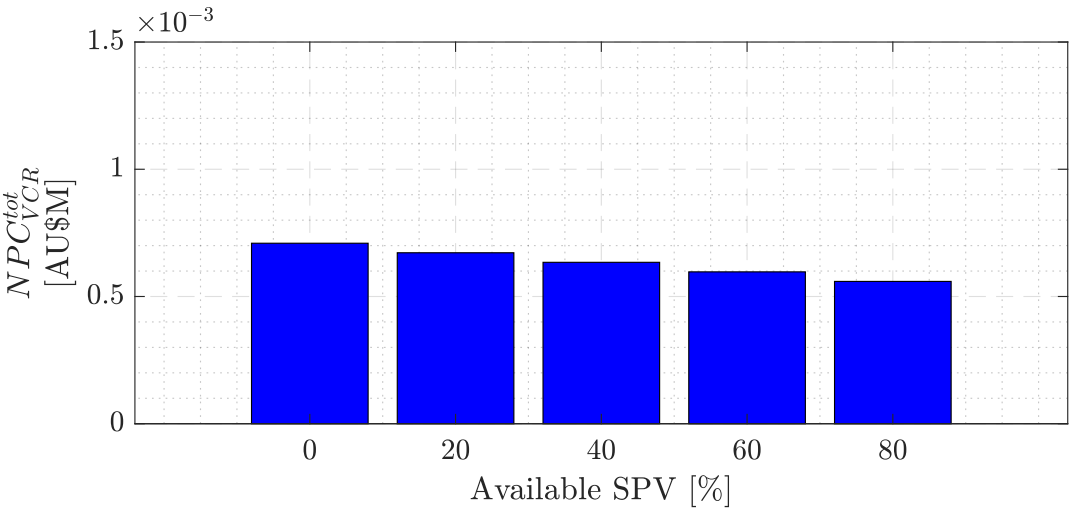

Figure 26: Results of NPC_{VCR}^{tot} during bushfire in grid-connected scenario of Tarnagulla network.

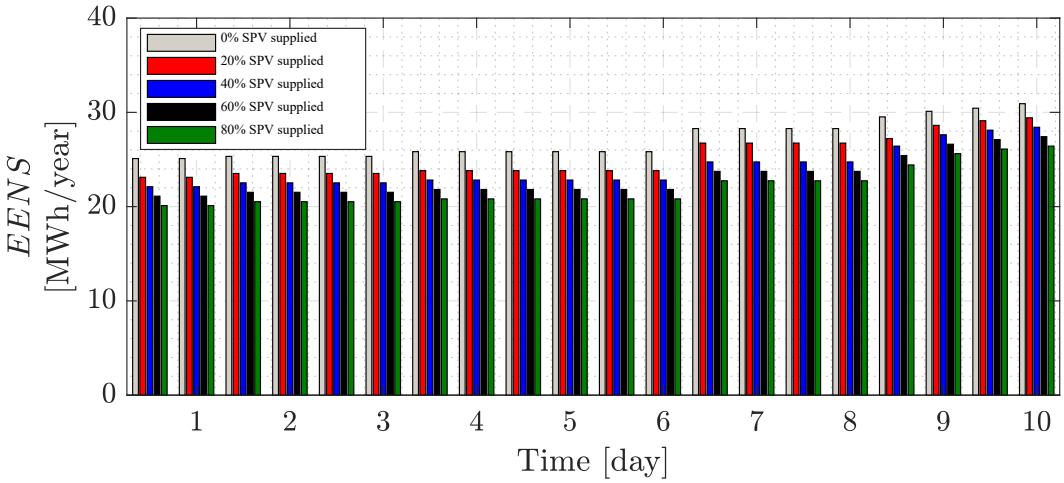

Figure 27: Results of $EENS$ during bushfire in off-grid scenario of Tarnagulla network.

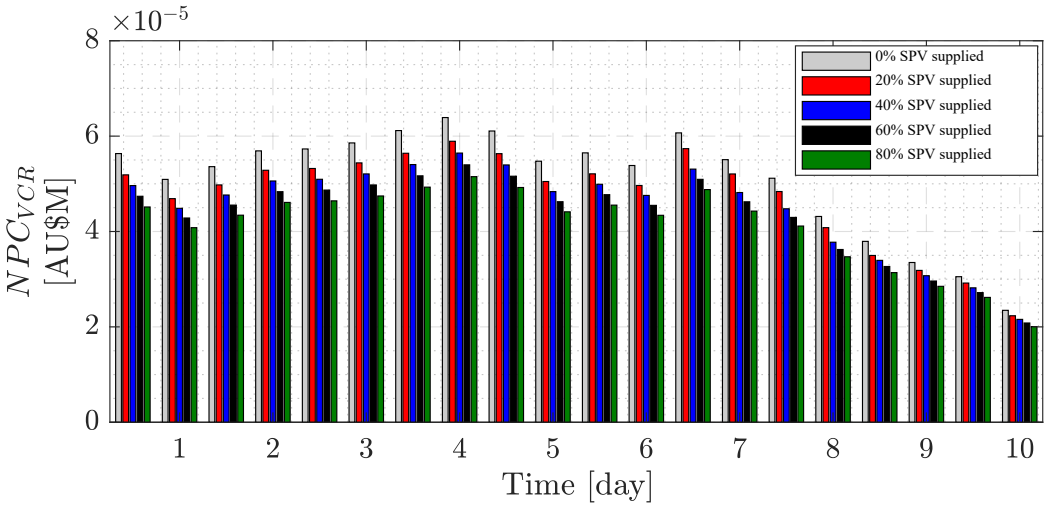

Figure 28: Results of NPV_{VCR} in each day during bushfire off-grid scenario of Tarnagulla network.

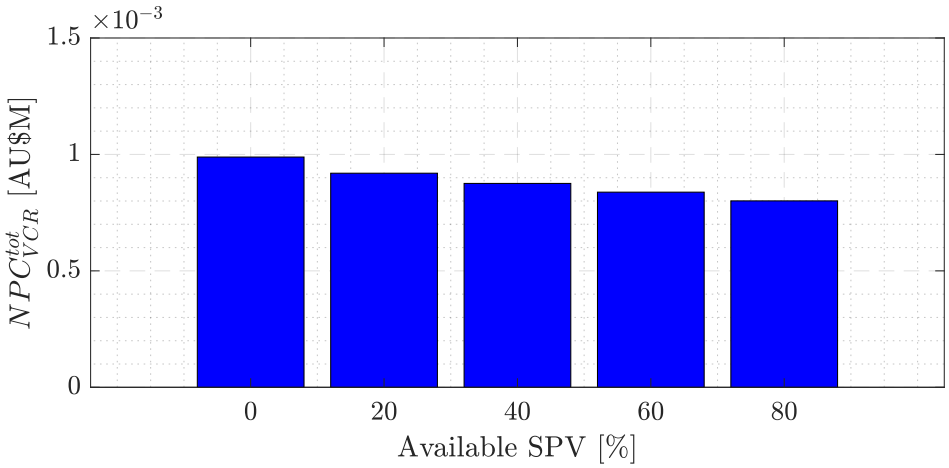

Figure 29: Results of NPC_{VCR}^{tot} during bushfire in off-grid scenario of Tarnagulla network.

Next, we have compared the network performance with the optimal size of the PV, DG and Battery obtained from techno-economic studies. Figure 30 shows the results for different penetrations of resources. The system would experience the lower EENS for the case with DER+EENS for all disturbance duration.

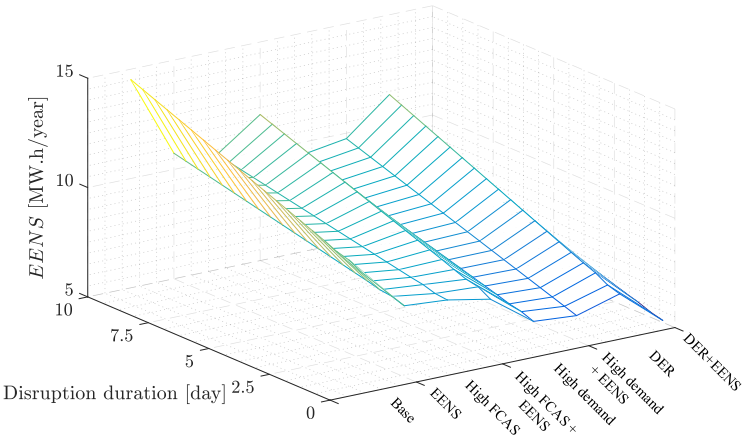

Figure 30: EENS in Tarnagulla network using optimal generation size obtained in techno-economic framework.

Figure 31 shows the EENS in the Tarnagulla network under volatile cases. From the results, we could see the lower EENS in the Tarnagulla network under DER+EENS case.

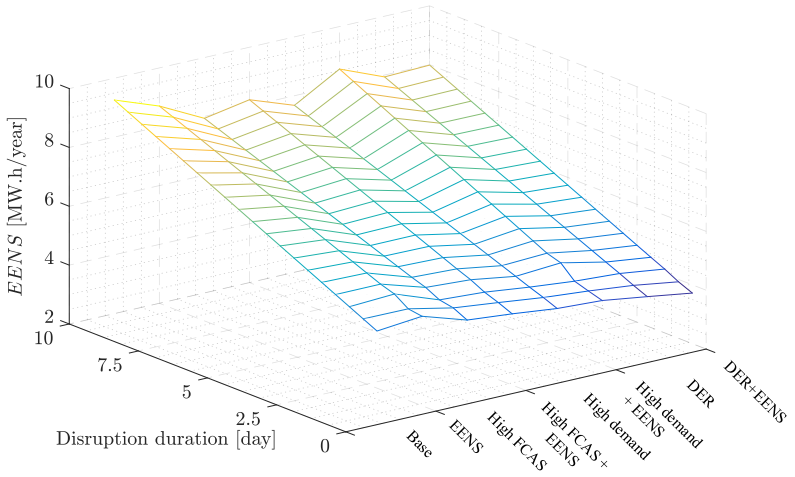

Figure 31. EENS under volatile cases of Tarnagulla network with optimal sizing the resources.

Further, sensitivity studies are conducted to assess the performance of the Tarnagulla network with the following scenarios and optimal generation size obtained:

- Two weeks of bushfire (no PV and battery) – case 1;
- Two weeks of bushfire with fuel disruption – Case 2;
- Normal operation and two weeks of bushfire – Case 3;
- Normal operation, two-week bushfire and fuel interruptions started from second week - Case 4;

Figure 32 shows the EENS of the network for the prior explained scenarios. From the results, it could be evident that the EENS of the system with normal operation is higher compared to the other cases. For case-4, the obtained resource allocation is high compared to the other cases (See Table 4).

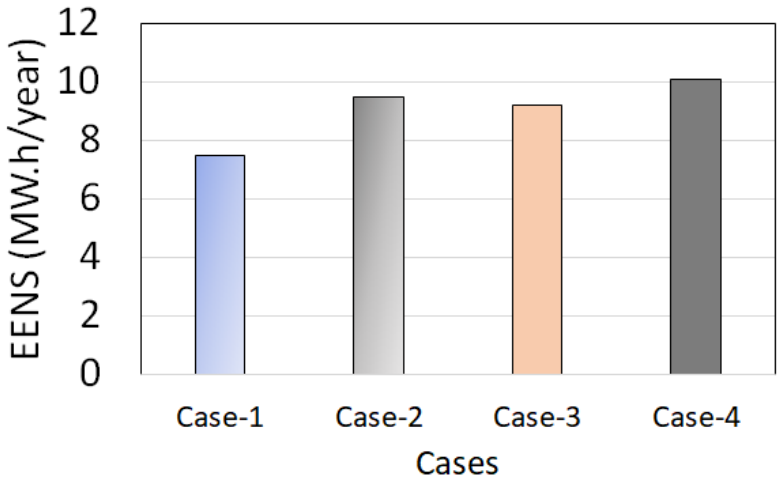

Figure 32. EENS of Tarnagulla system under different cases.

Table 7 Optimal generation size

Resources	Case -1	Case -2	Case -3	Case-4
Diesel (kW)	460	0	941	70
PV (kW)	0	4828	320	4851
Battery (Kw)	0	1255	408	1178

4.2. Results in the Donald Network

In this section, the reliability indices affected by the bushfire model are demonstrated. The Donald network is used to test the process. The network topology for the off-grid Donald network is referred to **Project 5**, scenario 16 in Table 1 with required generations as detailed in table 6. The same scenarios are conducted as mentioned in previous section, all conditions are the same as those of Figures 24, 26, 27, 28, and 29. Figures 33, 34, and 35 demonstrate the values of $EENS$, individual NPV_{VCR}, and NPC_{VCR}^{tot} in grid-connected Donald network, respectively. Figures 36, 37, and 38 show the values of $EENS$, individual NPV_{VCR}, and NPC_{VCR}^{tot} off grid Donald network, respectively. As can be seen, the value of $\mathrm{NPC}_{\mathrm{VCR}}^{\mathrm{tot}}$ under bushfire dynamic in the case of off-grid scenario is significantly higher than that of grid-connected scenario. In this light, for the individual NPV_{VCR}, this value depends on several factors such as the disruption duration, dis, and probability sets, $\mathbf{P}_{dd}^{dis}$. In some scenarios, with impacts of bushfire dynamic, the present NPV_{VCR} may be higher than the previous NPV_{VCR}. However, the power supplied from SPVs can significantly aid the capacity adequacy level, thus reducing the NPC_{VCR}^{tot}.

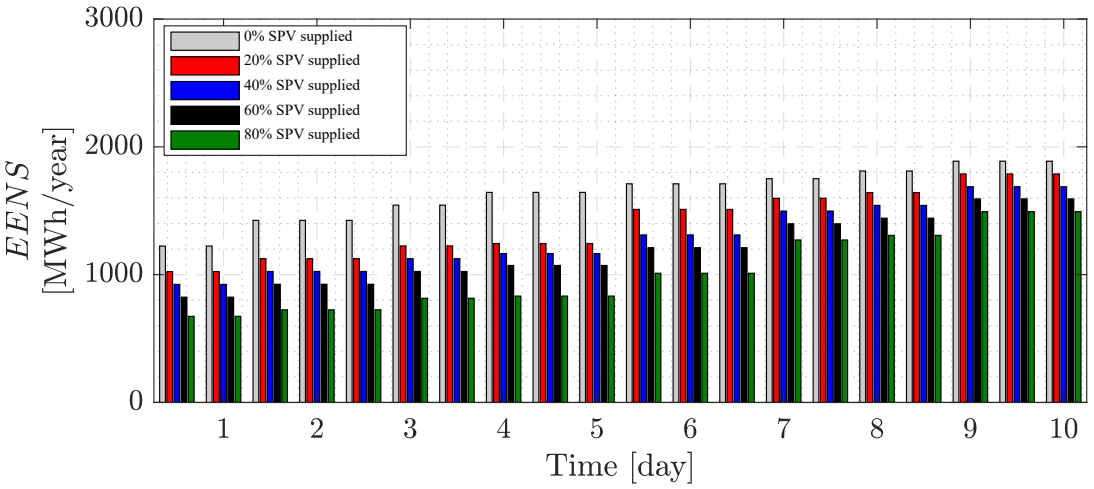

Figure 33: Results of $EENS$ during bushfire in grid-connected scenario of Donald network.

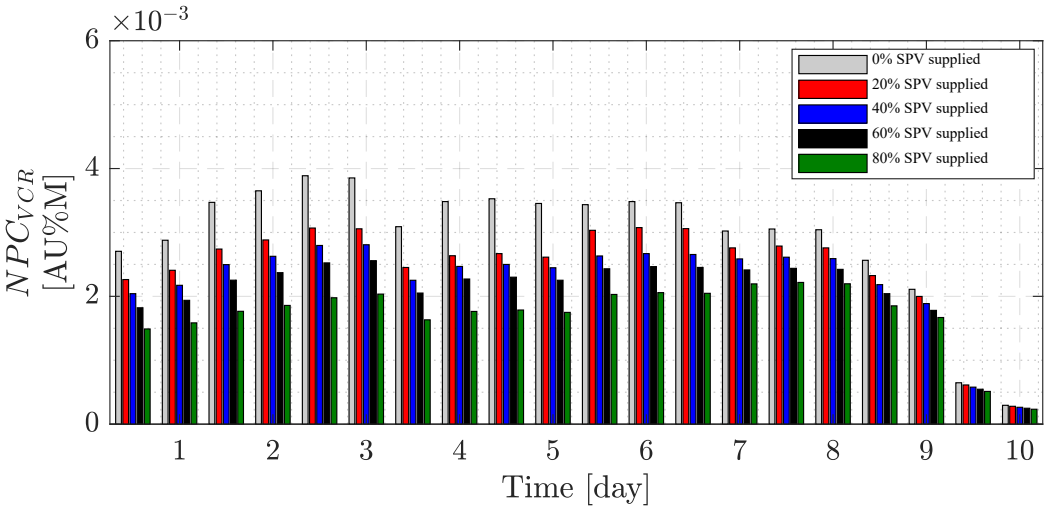

Figure 34: Results of NPV_{VCR} in each day during bushfire in grid-connected scenario of Donald network.

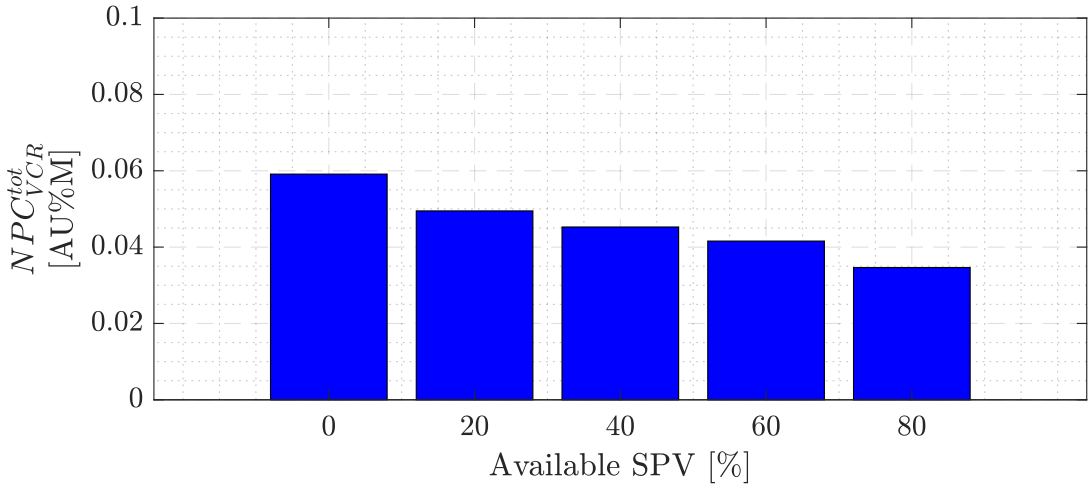

Figure 35: Results of NPC_{VCR}^{tot} during bushfire in grid-connected scenario of Donald network.

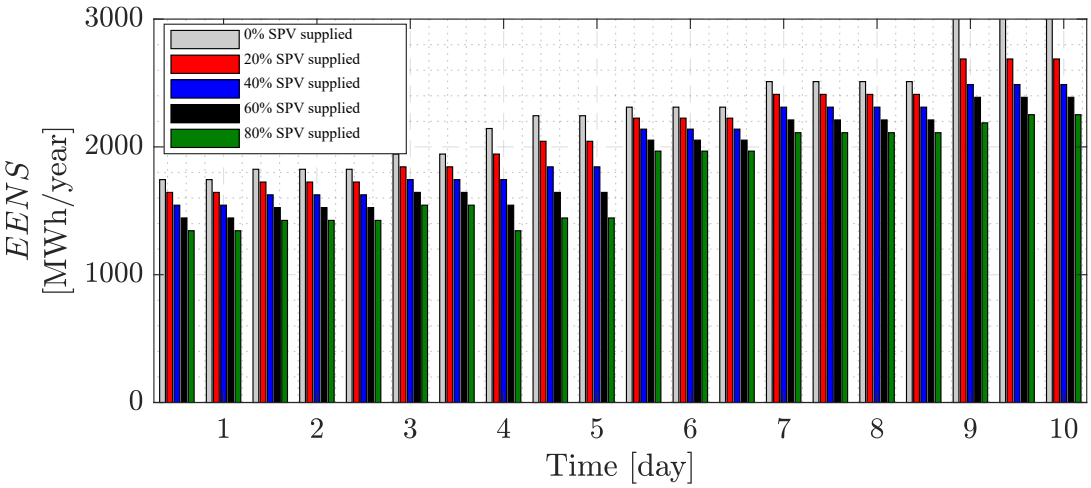

Figure 36: Results of $EENS$ during bushfire in off-grid scenario of Donald network.

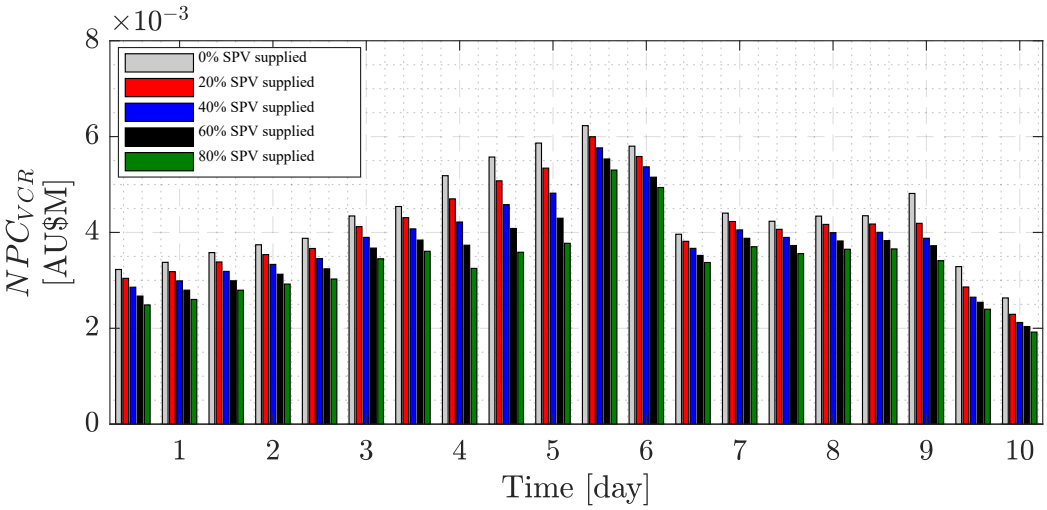

Figure 37: Results of NPV_{VCR} in each day during bushfire in off grid scenario of Donald network.

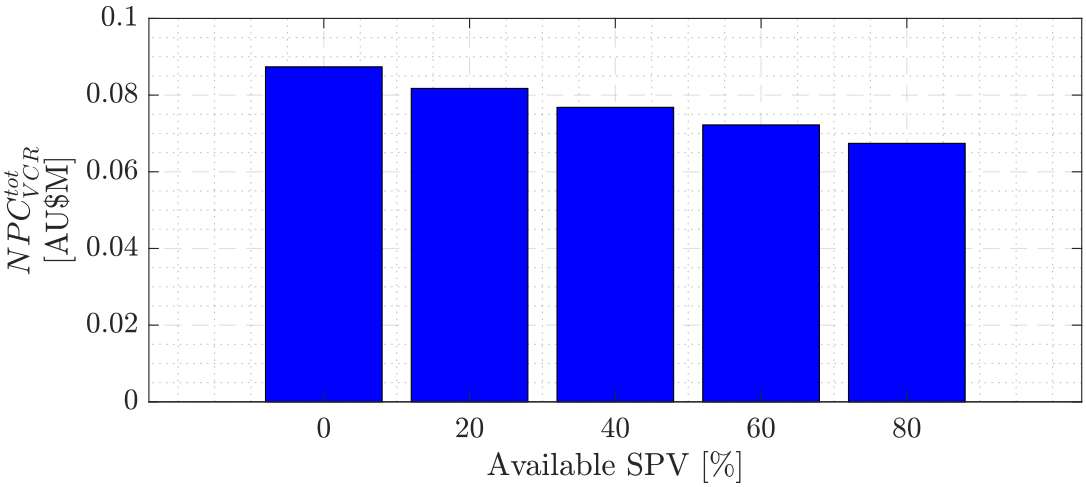

Figure 38: Results of NPC_{VCR}^{tot} during bushfire in off-grid scenario of Donald network.

Next, we have compared the network performance with the optimal size of the PV, DG and Battery obtained from techno-economic studies. Figure 39 shows the results for different penetrations of resources. The system would experience the lower EENS for the case with DER+EENS for all disturbance duration.

Figure 40 shows the EENS in the Donald network under volatile cases. From the results, we could see the lower EENS in the Tarnagulla network under DER+EENS case.

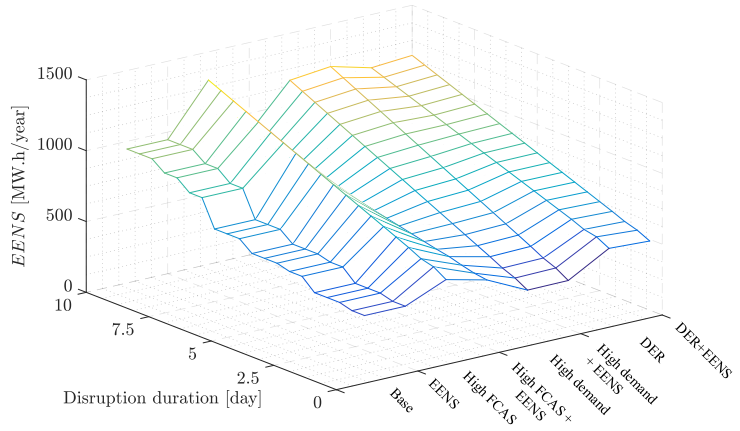

Figure 39: EENS in Donald network using optimal generation size obtained in techno-economic framework.

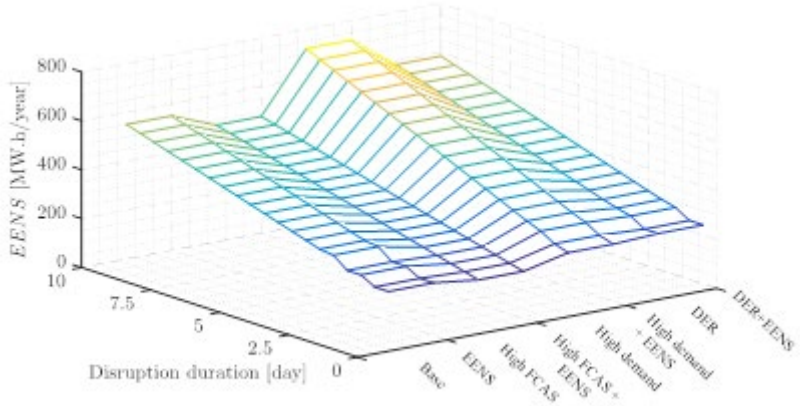

Figure 40. EENS under volatile cases of Donald network with optimal sizing the resources.

Furthermore, seven scenarios are obtained from each town's investment model ("Project 8: Economic and Risk Assessment – Part I"). These seven scenarios are further considered for microgrid and without microgrid cases in ("Project 8: Economic and Risk Assessment – Part I"). These scenarios are used for the economic risk valuation. The economic risk valuation for specific microgrids has been fed back to the investment model. For economic risk valuation, EENS value for each scenario has been compared by the research team with the base case for ten consecutive days to find out the implication of each generated scenario and then fed back to the investment modelling team. Then, the net present cost of the value of customer reliability is based on the expected energy not supplied. The detailed assessment results can be found in ("Project 8: Economic and Risk Assessment – Part I").

5. Estimation of Techno-Economic Risk Using Deep-Learning Neural Network

5.1. Application of Deep-Learning Neural Network for Parameter Estimations

In this project, two variables, i.e., $FFDI$ and wind speeds, are estimated to investigate the effects of bushfire dynamic. To estimate the day-ahead $FFDI$, the historical data projection is used as the input of the deep-learning neural network (DNN). The historical time-series data of $FFID$ and wind speed can be found in the following link: https://www.climatechangeinaustralia.gov.au/en/projects/esci/esci-climate-data/. The historical time-series data are collected from 1980 to 2022. However, only the data from 2019 to 2022 are used to train the DNN. Figure 41 shows an application of using deep-learning network for day-ahead $FFDI$ and wind speed estimation implemented in MATLAB [6]. For settings of the DNN, 150 iterations with 1000 epochs for each iteration are used to train the network, the hidden layer is set at 25. To train the network, 60%, 20%, 20% of the data are used for the training, validating, and testing stages, respectively. To estimate the $FFDI$, we use *i)* the actual $FFDI$ data of previous 14 days, *ii)* month index (i.e., 1, 2, 3, …,12), and *iii)* rate of change of $FFDI$ $\left(=\frac{\Delta FFDI}{\Delta t}\right)$ as the inputs to estimate a day-ahead $FFDI$ (an output). In the same way, to estimate the wind speed, we use *i)* the actual wind speed data of previous 14 days, *ii)* month index (i.e., 1, 2, 3, …,12), and *iii)* rate of change of wind speed $\left(\frac{\Delta \bar{V}_w}{\Delta t}\right)$ as the inputs to estimate a day-ahead wind speed (an output). The rates of changes $\frac{\Delta FFDI}{\Delta t}$ and $\frac{\Delta \bar{V}_w}{\Delta t}$ are the physics-informed data that are used to guide the training process of the DNN, thus improving the accuracy of the estimation [7]. By using such inputs, this DNN is defined as the physics-informed DNN. As a result, the physics-informed DNN is classified as multi-input single-output DNN.

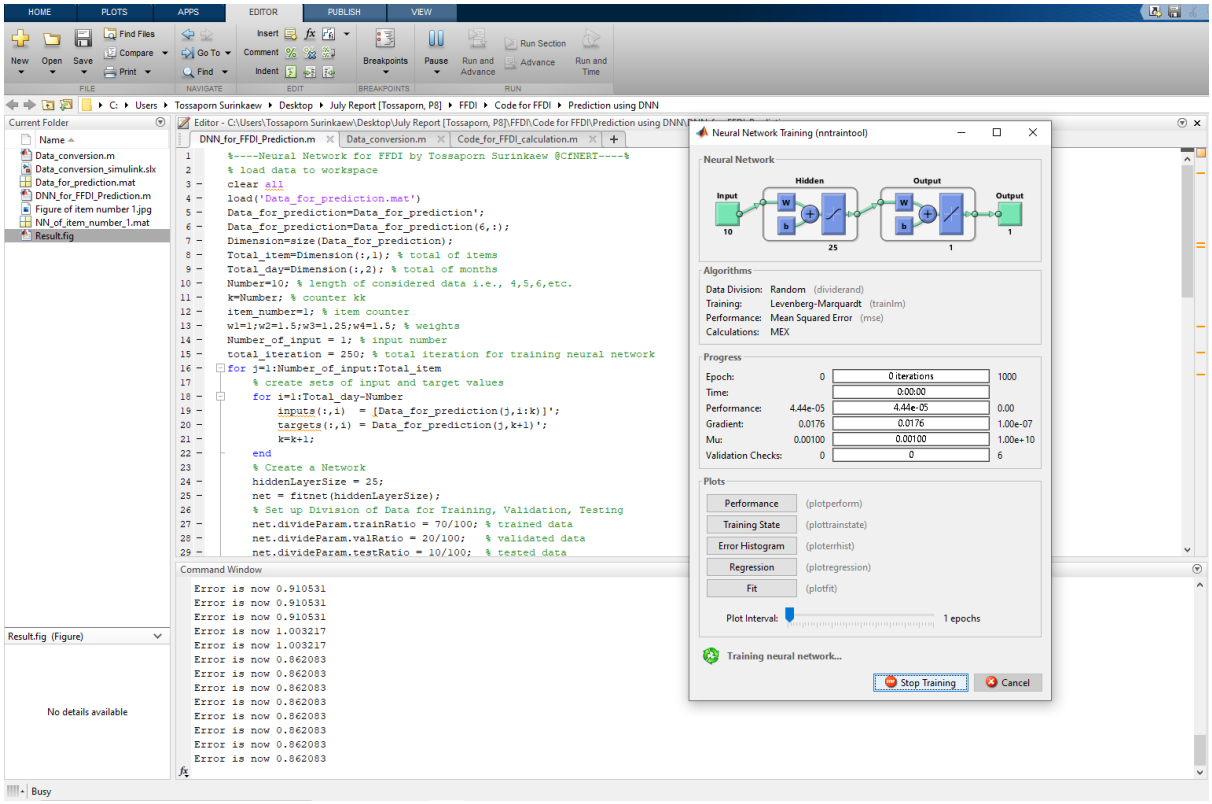

Figure 41: MATLAB-mfile-based DNN toolbox for day-ahead $FFDI$ and related parameter estimations.

After the training, validating, and testing stages, Figures 42, 43, and 44 demonstrate the performance of the trained DNN for day-ahead $FFDI$, line failure, and estimation error, respectively. In Figures 43 and 44, performance of the physics-informed DNN is compared with conventional DNN, which uses only historical data as the input. As can be seen the physics-informed DNN provide better accuracy of the estimation. As a result, the physics-informed DNN is used to estimate the $FFDI$ and wind speeds. Figure 44 shows the estimated wind speed. Overall, the estimated values are close to actual data. Thus, the trained physics-informed DNN can achieve very high accuracy to estimate day-ahead $FFDI$ and wind speed for further analysis. In Figure 37, is can be seen that the $FFDI$ is less than 11 during May to October. Since the line failure rate is constant when the $FFDI < 11$, the summer time (around November 2021 – April 2022, $FFDI \geq 11$) is used to analyse the bushfire dynamic in this section.

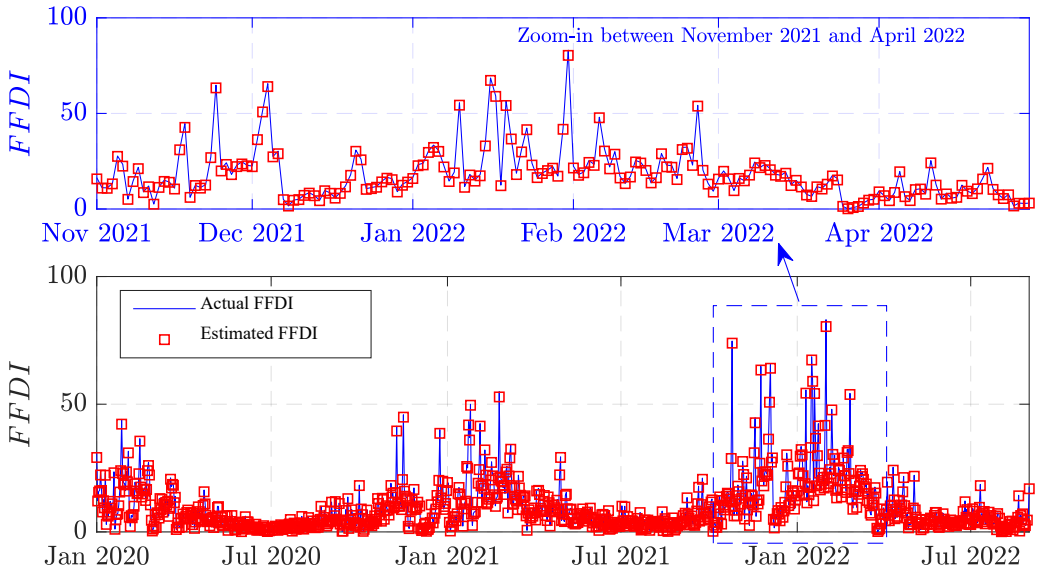

Figure 42: Estimated $FFDI$ using physics-informed DNN.

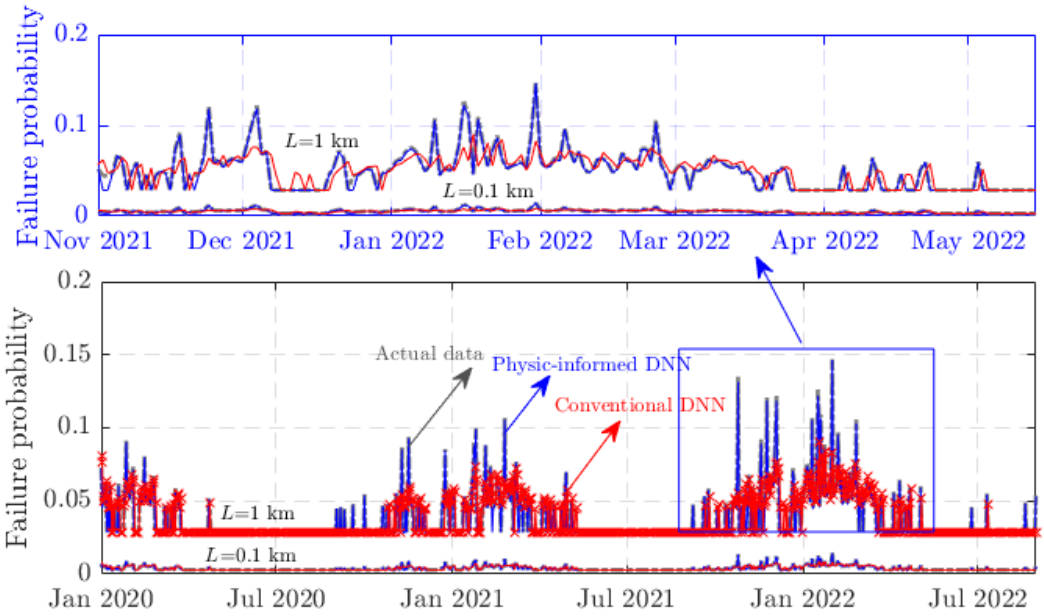

Figure 43: Comparison of failure probability using different estimation methods.

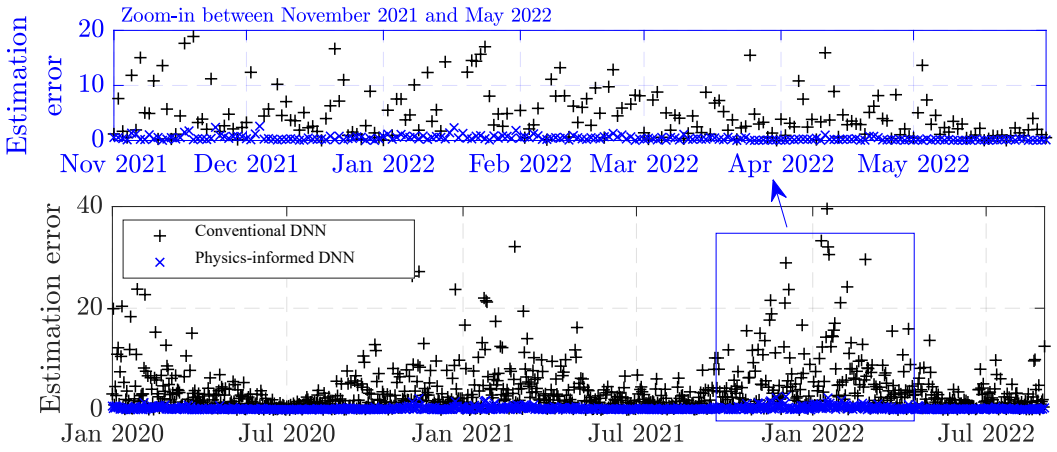

Figure 44: $FFDI$ estimation errors using different estimation methods.

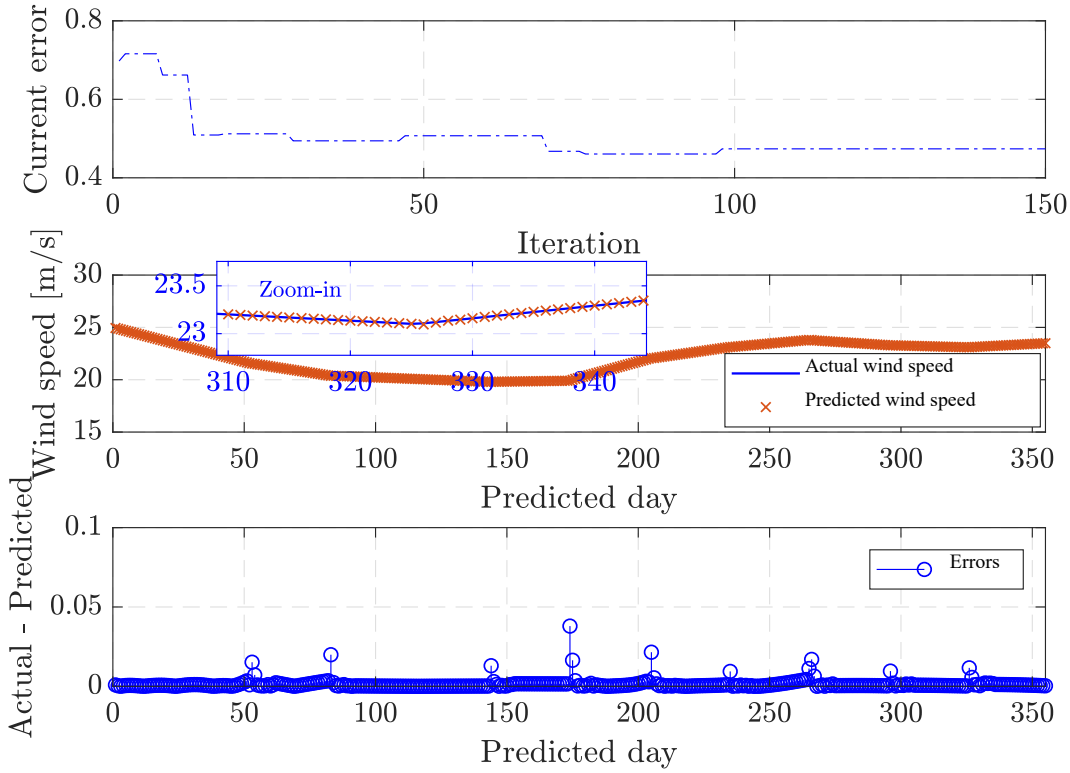

Figure 45: Wind speed estimation using DNN.

5.2. *N*-Day-ahead Techno-economic Risk Indices Using Estimated Data

After the training process, the trained DNN is used to evaluate N-day-ahead $EENS$ and NPV_{VCR} considering uncertainties of SPV supported powers. Here, N represents the period from summer time (01 November 2022 to 30 April 2023). In additional, different types of loads are considered for the different values of $\mathbf{VCR}_{dd}^{initial}$ (see (25) - (30)). According to [5], $VCR_{dd}^{initial,res} = \frac{22.58\$}{\text{kWh}}$, $VCR_{dd}^{initial,com} = \frac{46.18\$}{\text{kWh}}$, and $VCR_{dd}^{initial,ind} = \frac{66.16\$}{\text{kWh}}$. In this study, the ratios $\left[\frac{s_L^{res}}{s_L^{tot}}, \frac{s_L^{com}}{s_L^{tot}}, \frac{s_L^{ind}}{s_L^{tot}}\right]$ are set by [0.7,0.2,0.1] and the sensitivity of line failure is set at $\boldsymbol{m} = m_5 = 5\%$. Here, the probability sets for supply disruption duration

are assumed to be 100 different scenarios, i.e., $\mathbf{P}_{dd}^{dis} = \mathrm{sort}\left(\mathrm{rand}\left(100, \mathrm{length}(dis)\right)\right)$. After using the estimated data in Figures 42 and 45, and (25) – (30), Figures 46, 47, and 48 respectively show the mean results of $EENS$, NPV_{VCR}, and NPC_{VCR}^{tot} under 100 different probability sets using the estimated data in off-grid scenario of the Donald network while Figures 49, 50, and 51 respectively demonstrate the same techno-economic indices in the Tarnagulla network. For the grid-connected scenarios, Figures 52, 53, and 54 respectively show the mean results of $EENS$, NPV_{VCR}, and NPC_{VCR}^{tot} under 100 different probability sets using the estimated data in grid-connected scenario of the Donald network while Figures 55, 56, and 57 respectively demonstrate the same techno-economic indices in the Tarnagulla network. Note that the historical data in previous years are used to estimate the $FFDI$ and wind speed in the next year. These results show the estimated techno-economic reliability indices of N-day-ahead (01 November 2022 to 31 May 2023).

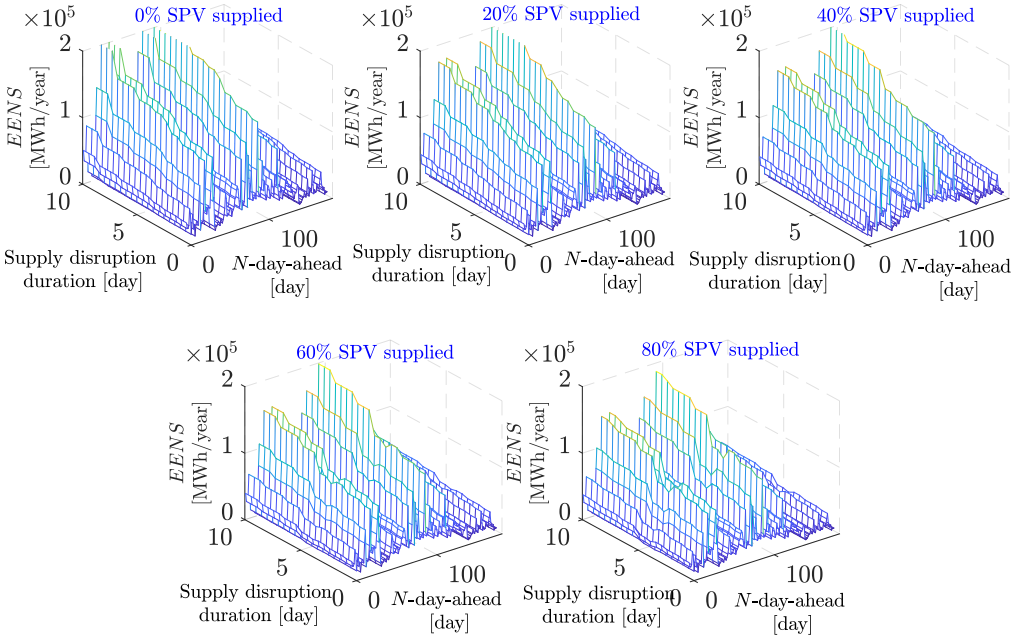

Figure 46: Results of $EENS$ in N-day-ahead during bushfire in off-grid scenario of Donald network.

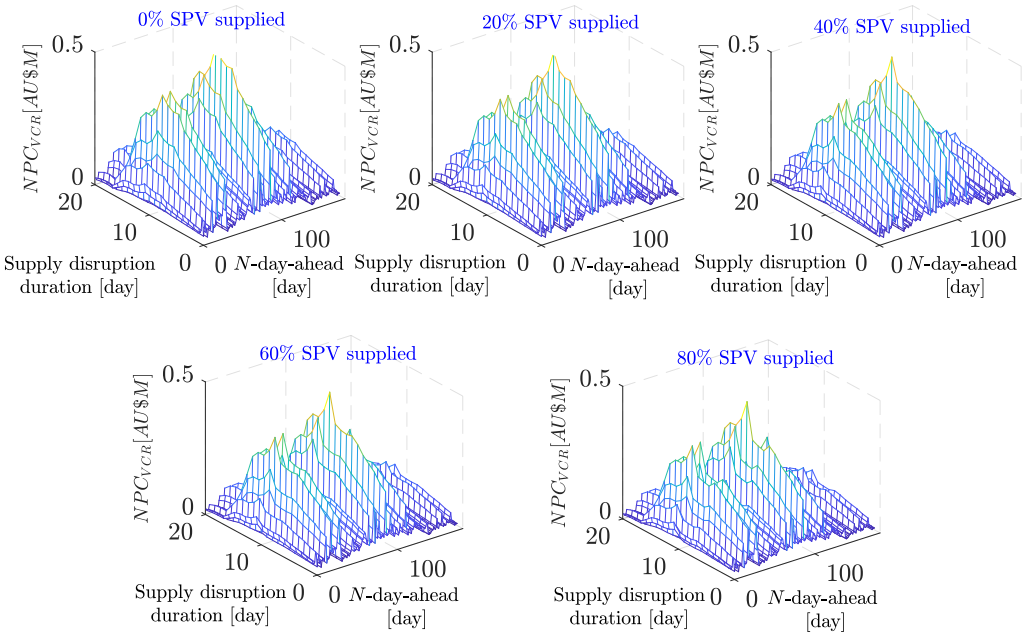

Figure 47: Results of NPV_{VCR} in N-day-ahead during bushfire in off-grid scenario of Donald network.

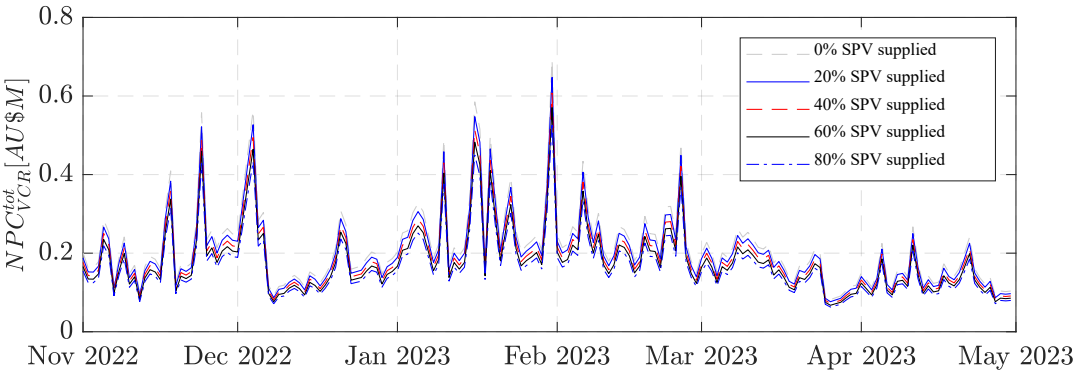

Figure 48: Results of NPC^{tot}_{VCR} in N-day-ahead during bushfire in off-grid scenario of Donald network.

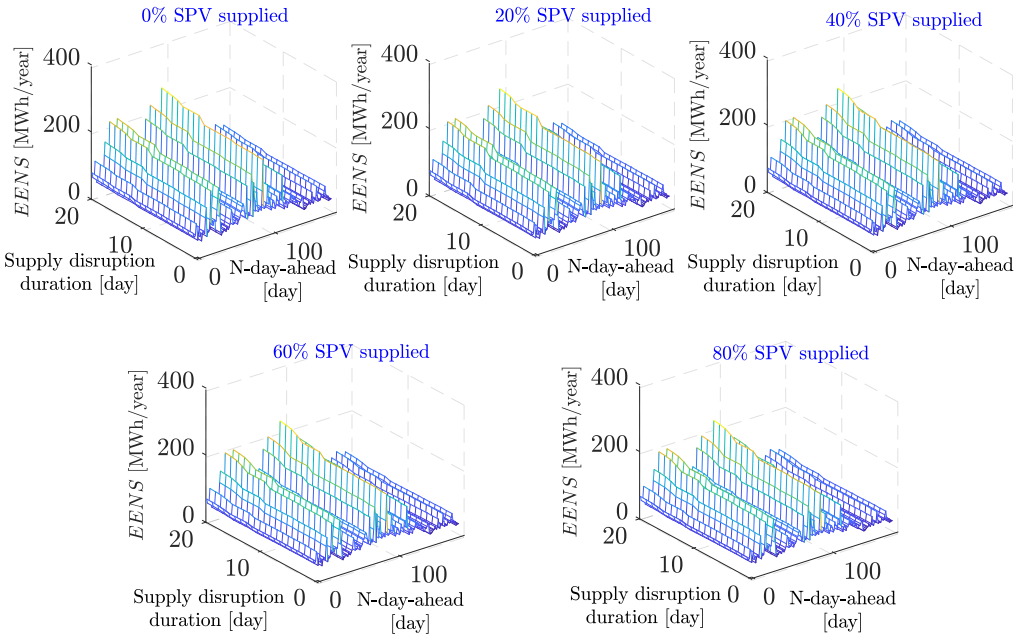

Figure 49: Results of $EENS$ in N-day-ahead during bushfire in off-grid scenario of Tarnagulla network.

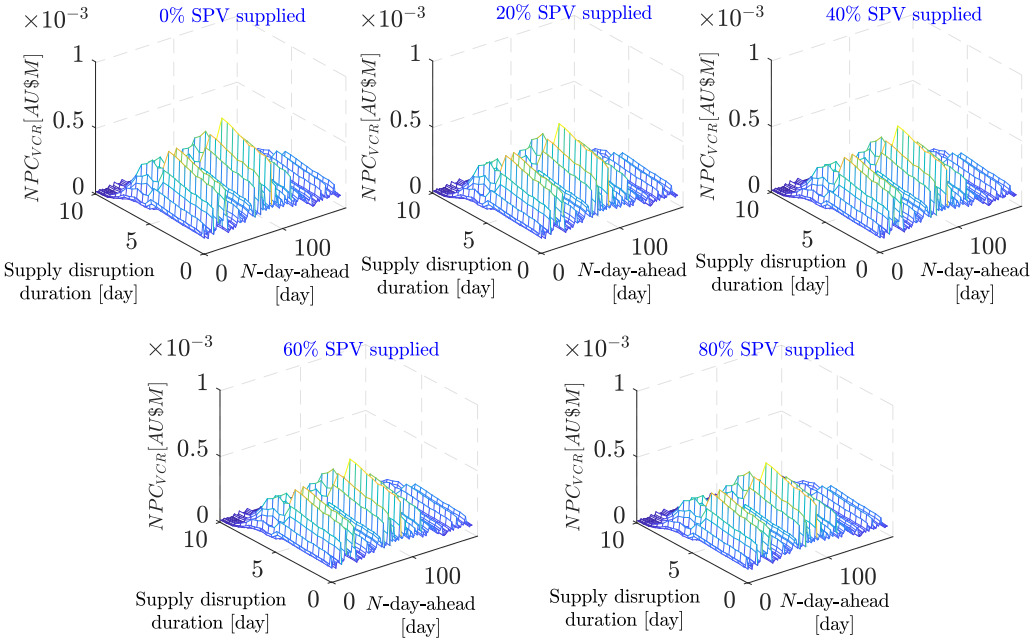

Figure 50: Results of NPV_{VCR} in N-day-ahead during bushfire in off-grid scenario of Tarnagulla network.

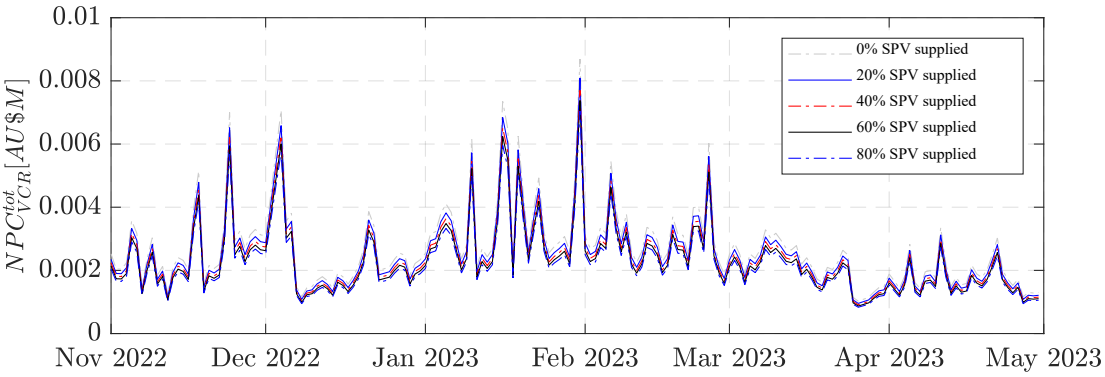

Figure 51: Results of NPC_{VCR}^{tot} in N-day-ahead during bushfire in off-grid scenario of Tarnagulla network.

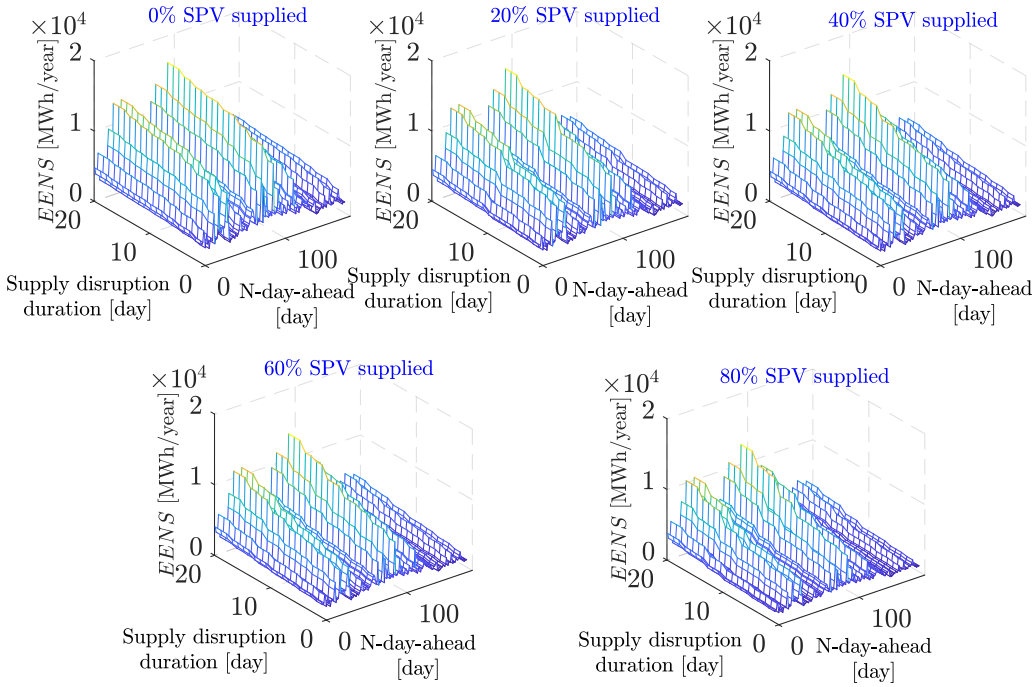

Figure 52: Results of $EENS$ in N-day-ahead during bushfire in grid-connected scenario of Donald network.

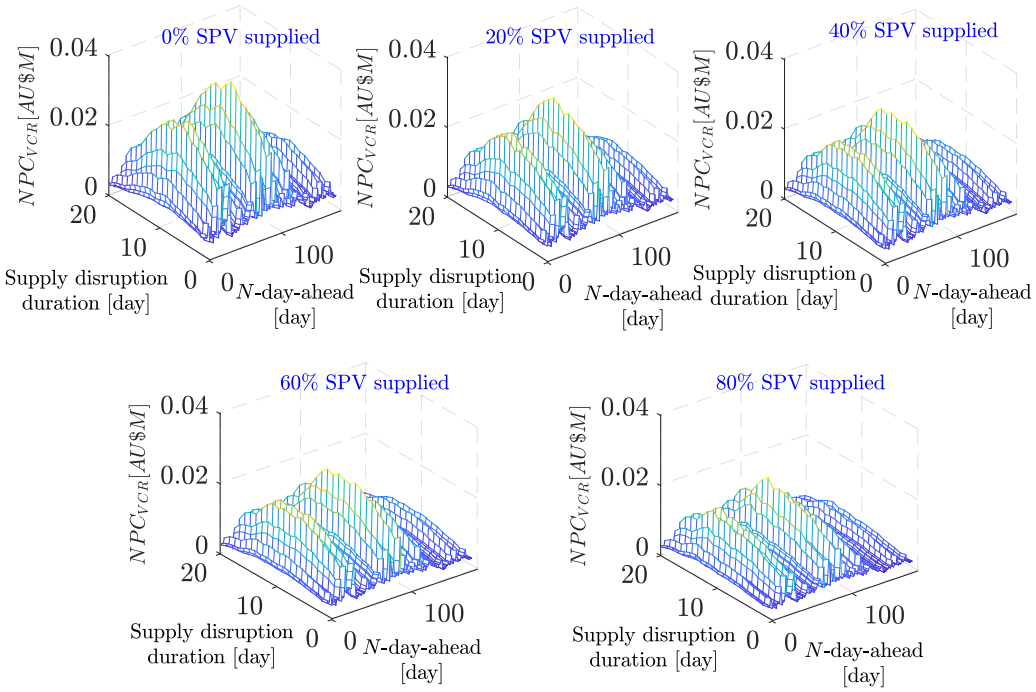

Figure 53: Results of NPV_{VCR} in N-day-ahead during bushfire in grid-connected scenario of Donald network.

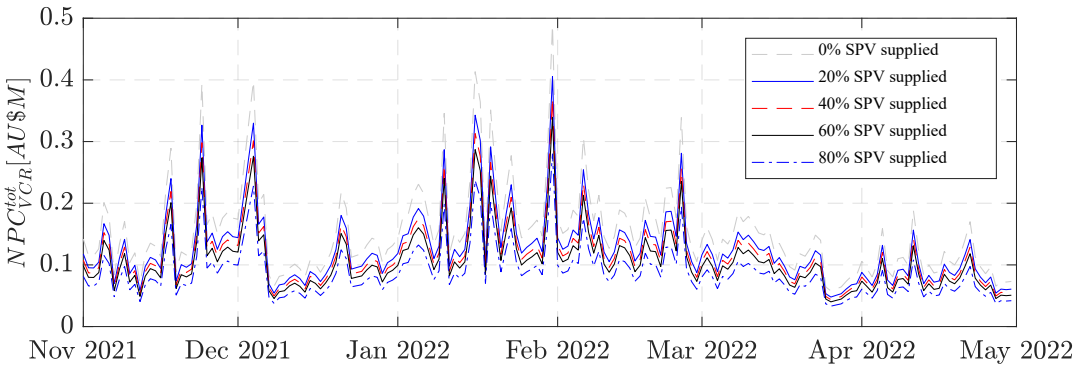

Figure 54: Results of NPC^{tot}_{VCR} in N-day-ahead during bushfire in off-grid scenario of Donald network.

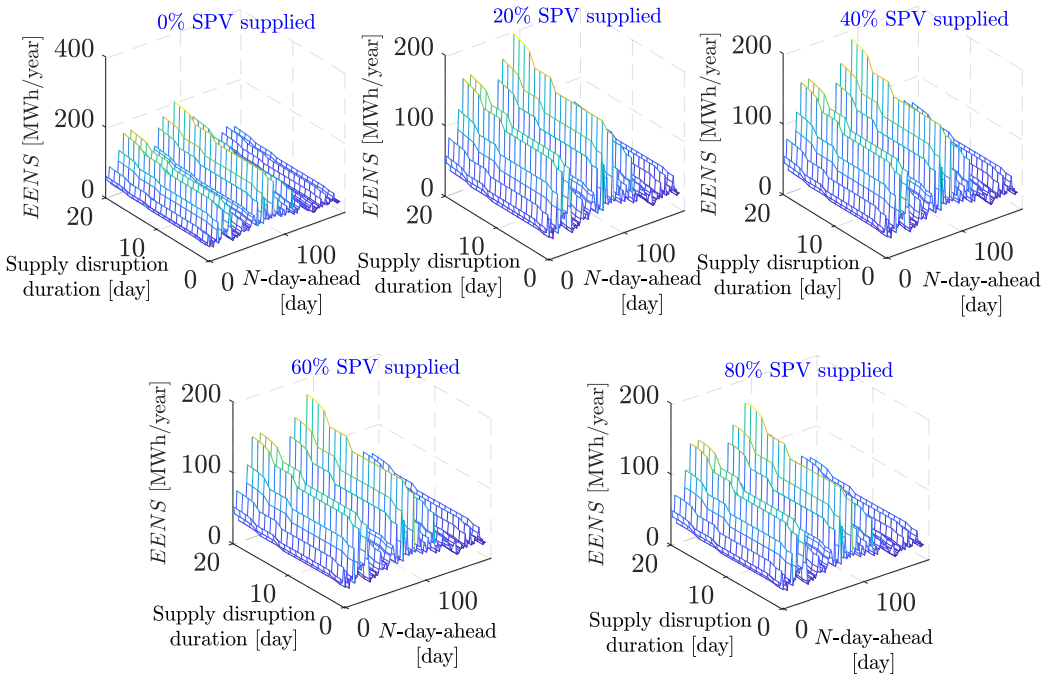

Figure 55: Results of $EENS$ in N-day-ahead during bushfire in grid-connected scenario of Tarnagulla network.

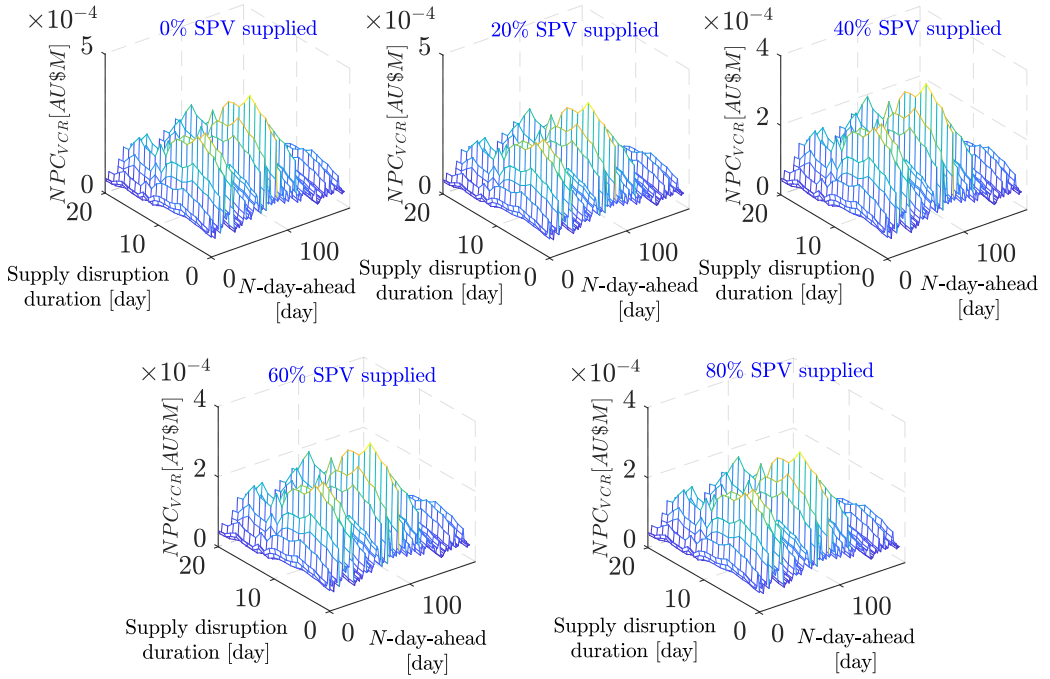

Figure 56: Results of NPC_{VCR} in N-day-ahead during bushfire in grid-connected scenario of Tarnagulla network.

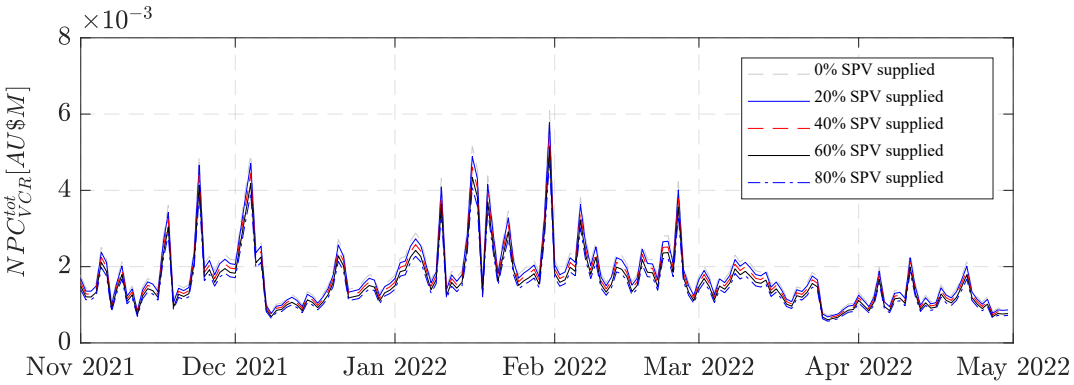

Figure 57: Results of NPC_{VCR}^{tot} in N-day-ahead during bushfire in grid-connected scenario of Tarnagulla network.

6. Summary

This report ("Project 8: Economic and Risk Assessment – Part II") presents the work performed by the Federation University Australia focused on network reliability and the impact of bushfires in each town. This work mainly focused on the detailed modeling of distribution network reliability assessment techniques, to value the techno-economic risk associated with microgrid users for different planning alternatives and types of events (e.g., bushfires). This model is then used to assess the reliability performance of the system with optimal generation determined in Part I. The economic risk valuation for specific microgrids has been fed back to the investment model for comparison. The comparative results are given in project report ('Project 8: Economic and Risk Assessment – Part I').

Furthermore, the impacts of firestorm dynamic on the techno-economic risk-based assessment are thoroughly investigated for Donald and Tarnagulla. A new intelligent-based framework is proposed to evaluate the risks due to firestorms and their dynamics. The innovations and important findings are summarized as follows:

1) New mathematical equations are developed in this paper to *i)* model the firestorm dynamic for the reliability assessment in distribution systems or microgrids, the firestorm dynamics relate to wind speeds and their directions while the firestorm effects involve with the forest fire danger index (known as $FFDI$), and *ii)* deeply analyse the firestorm dynamics under possible supply disruption durations, which may lead to *N - K* outage contingency,
2) The proposed framework effectively evaluates the risk indices due to the firestorm under various conditions, thus allowing enough time to seek suitable/resilient countermeasures to mitigate them.

For our future works, optimal sizes of distributed generations considering system constraints will be conducted to minimise the firestorm effects under various grid conditions, such as grid-connected/islanding scenarios. Moreover, possible strategies such as identifying the load criticality, forecasting the future loads/generations, and investigating the impacts of converter-controlled-based resources can be incorporated into the proposed intelligent-based strategy to predict the risk indices more accurately.

Reference

[1] Noble, I. R., Gill, A. M., & Bary, G. A. V. (1980). McArthur's fire-danger meters expressed as equations. *Australian Journal of Ecology*, *5* (2), 201-203.

[2] Finkele, K., Mills, G. A., Beard, G., & Jones, D. A. (2006). National gridded drought factors and comparison of two soil moisture deficit formulations used in prediction of Forest Fire Danger Index in Australia. *Australian Meteorological Magazine*, *55* (3), 183-197.

[3] Dolling, K., Chu, P. S., & Fujioka, F. (2005). A climatological study of the Keetch/Byram drought index and fire activity in the Hawaiian Islands. *Agricultural and Forest Meteorology*, *133* (1-4), 17-27.

[4] National Electricity Amendment (Regulated stand-alone power systems) Rule 2022, Clause 5.10.2.

[5] Australian Energy Regulator, Values of Customer Reliability adjusted for 2021, https://www.aer.gov.au/communication/values-of-customer-reliability-adjusted-for-2021

[6] Kim, Phil. "Matlab deep learning." *With machine learning, neural networks and artificial intelligence* 130.21 (2017).

[7] Raissi, Maziar, Paris Perdikaris, and George E. Karniadakis. "Physics-informed neural networks: A deep learning framework for solving forward and inverse problems involving nonlinear partial differential equations." *Journal of Computational physics* 378 (2019): 686-707.